MANUSCRIPT 5612: REVISION 1.

An X-ray magnetic circular dichroism (XMCD) study of Fe ordering in a synthetic $MgAl_2O_4$ – Fe_3O_4 (spinel – magnetite) solid solution series; implications for magnetic properties.

Running title: Cation site ordering in spinel – magnetite solid solutions

C. Michael B. Henderson[1,2], Carolyn I. Pearce[1,3,5], John M. Charnock[1], Richard J. Harrison[4] and Kevin M. Rosso[1,5]

[1] Williamson Research Centre, School of Earth, Atmospheric and Environmental Sciences, University of Manchester, Manchester M13 9PL, U.K.

[2] Astec, Daresbury Laboratory, STFC, Warrington WA4 4AD, U.K.

[3] School of Chemistry and Dalton Nuclear Institute, University of Manchester, M13 9PL, U.K.

[4] Department of Earth Sciences, University of Cambridge, CB2 3EQ, UK.

[5] Pacific Northwest National Laboratory, Richland, WA 99352, USA.

ABSTRACT

Fe $L_{2,3}$-edge XAS and XMCD studies have been used to unravel structural trends in the $MgAl_2O_4$–Fe_3O_4 solid solution where thermodynamic modelling has presented a challenge due to the complex ordering arrangements of the end-members. Partitioning of Fe^{3+} and Fe^{2+} between tetrahedral (Td) and octahedral (Oh) sites has been established. In the most Fe-rich samples, despite rapid quenching from a disordered state, Fe^{2+}_{Td} is not present, which matches the ordered, inverse spinel nature of end-member magnetite (Mgt) at room-T. However, in intermediate compositions Al and Mg substantially replace Fe and small amounts of Fe^{2+}_{Td} are found, stabilized or trapped by decreasing occurrence of the continuous nearest neighbour Fe – Fe interactions which facilitate charge redistribution by electron transfer. Furthermore, in the composition range ~$Mgt_{0.4\text{-}0.9}$, XAS and XMCD bonding and site occupancy data suggest that nano-scale, magnetite-like Fe clusters are present. By contrast, at the spinel-rich end of the series, $Mgt_{0.17}$ and $Mgt_{0.23}$ have a homogeneous long-range distribution of Fe, Mg and Al. These relationships are consistent

with the intermediate and Fe-rich samples falling within a wide solvus in this system such that the Fe-clusters occur as proto-nuclei for phases which would exsolve following development of long-range crystalline order during slow cooling.

Unit cell edges calculated from the spectroscopy-derived site occupancies show excellent agreement with those measured by X-ray powder diffraction on the bulk samples. Calculated saturation magnetic moments (M_s) for the Fe-rich samples also show excellent agreement with measured values but for the most Mg-rich samples are displaced to slightly higher values; this displacement is due to the presence of abundant Mg and Al disrupting the anti-parallel alignment of electron spins for Fe atoms.

Keywords: $MgAl_2O_4$-Fe_3O_4 spinel solid solutions; Fe $L_{2,3}$ X-ray absorption spectroscopy; Fe $L_{2,3}$ X-ray magnetic circular dichroism; Mg and Fe *K*-edge extended X-ray absorption fine structure spectroscopy; octahedral and tetrahedral site occupancies; calculated unit cell parameters; calculated magnetic moments; spinel-magnetite solvus; hypothetical high-temperature ordering model.

INTRODUCTION

Spinel group samples ($M^{2+}M^{3+}{}_2O_4$, where M^{2+} = Mg, Mn, Fe, Co, Ni, Cu, Zn and M^{3+} = Al, V, Cr, Mn, Fe, Co) can occur as end-members or as intermediate compositions in various solid solution series. Fe-rich analogues (ferrites) are particularly noteworthy for possessing the characteristic property of ferrimagnetism. Because of their physical and electronic properties, they are widely used as technological and medical materials (e.g., magnetic recording media, batteries, catalysts, gas sensors, pigments, pharmaceuticals and magnetic resonance imaging 'targets'). The superparamagnetic properties of ferrite nanoparticles are the subject of expanding research (Pellegrin et al., 1999; Liu et al., 2000; Gunjakar et al., 2008; Pearce et al., 2012; Byrne et al., 2013; Tiano et al., 2015). The most common natural spinel is magnetite ($Fe^{2+}Fe^{3+}{}_2O_4$) but other minerals include spinel (*ss*, $MgAl_2O_4$), and complex solid solutions (e.g., franklinite $(Mn,Fe,Zn)^{2+}(Fe,Mn)^{3+}{}_2O_4$). Titanomagnetite occurs naturally as solid solutions between magnetite and ulvőspinel ($Fe^{2+}{}_2TiO_4$); oxidized analogues of Fe^{2+}-bearing spinels are also known (e.g., maghemite $Fe^{3+}{}_{2.666}\square_{0.333}O_4$ (γ-Fe_2O_3)). Such minerals are of key importance in the Earth Sciences as the magnetic properties of rocks are dominated by the presence of the ferrimagnetic minerals titanomagnetite, magnetite, maghemite and hemo-ilmenite.

Comprehensive reviews of the crystal chemistry and structure of spinels are given in Lindsley (1976), Hill *et al*. (1979), Waychunas (1991), and Bowes *et al.* (2011). The oxygens define an essentially face-centred, cubic close-packed array; the spinel unit cell, with 32 oxygens, has 64 tetrahedral (Td) sites and 32 octahedral (Oh) sites. Only 1/8 of the Td sites (denoted equipoint 8*a*, A sub-lattice) and ½ of the Oh sites (denoted 16*d*, B sub-lattice) are occupied, giving the unit cell formula $A_8B_{16}O_{32}$ (i.e. Z = 8 AB_2O_4). However, excess metal cations may occupy normally vacant interstitial sites to form defect solid structures (Fleet, 1981, 1982). The net magnetization of ferrite spinels results from Fe in the A – B sites having unpaired electron spins of unequal magnetic moment below the Curie temperature, which are aligned exactly antiparallel to each other (Néel, 1955); A – B interactions are much stronger than B – B and A – A interactions.

The spinel aristotype structure is cubic *Fd3m* with a cell geometry fully defined by the oxygen positional parameter (*u*) which has unique atomic coordinates of exactly 0.2500, 0.2500, 0.2500 when the oxygens are perfectly cubic close-packed. The unit cell edge (*a*) reflects the relative sizes of cations occupying the different sites and thus the distribution of each cation species between the octahedral and tetrahedral sites. *Normal* spinels are characterized by the cation distribution $(M^{2+})^A(M^{3+}M^{3+})^BO_4$ and *inverse* spinels by$(M^{3+})^A(M^{2+}M^{3+})^BO_4$. Most spinels show non-convergent disorder of cations over the tetrahedral and octahedral sites and can be described using an inversion parameter (*x*) and the formula $(M^{2+}_{1-x}M^{3+}_{x})^A(M^{2+}_{x}M^{3+}_{2-x})^BO_4$ where $x = 0$ for an end-member normal spinel and $x = 1$ for a completely inverse spinel. A fully disordered spinel would have $x = 0.666$ for both A and B sites.

Clearly it is necessary to determine element valences and site occupancies in order to assess the physical properties of members of the spinel group; this is frequently a challenge in simple end-member spinels but is even more difficult for chemically-complex solid solutions. In this paper we present room-T, high-resolution Fe $L_{2,3}$ XMCD data for a rapidly quenched, synthetic spinel ($MgAl_2O_4$) – magnetite (Fe_3O_4) series; Harrison and Putnis (e.g., 1995, 1996, 1997a) have published extensively on the magnetic properties of these samples and have interpreted high-T, neutron powder diffraction data on cation ordering for three intermediate compositions (Harrison and Putnis, 1999). In this new work, we pay particular attention to the possibility of non-stoichiometry in the samples (i.e., presence of an excess or deficiency of metal cations). Calculation of cubic unit cell parameters from the adopted site occupancies (*cf* Marshall and Dollase, 1984;

Henderson *et al*., 2007) and comparing them to measured values will allow assessment of whether these occupancies match those for the bulk samples. The adopted data are compared to the high-T cation occupancy data of Harrison and Putnis (1999) and to those of Nell et al. (1989) and Nell and Wood (1989), which were based on thermo-power and conductivity measurements. In addition, the implications of our new data to the magnetic properties for this spinel solid-solution series are considered.

Cation site occupancies, unit cell edges and implications to magnetic properties.

X-ray and neutron diffraction (XRD and ND) have frequently been used to determine ordering of atoms over structurally distinct crystallographic sites but the data are only unambiguous for binary metal compounds and where the scattering properties of the two metals are sufficiently different. For example, XRD study has provided reliable data for the ordering of Mg and Fe^{3+} between Oh and Td sites in $MgFe_2O_4$ spinel (Nakatsuka et al., 2004) while ND methods defined equivalent data for Ni and Cr in $NiCo_2O_4$ spinel (Marco et al., 2001) and for Mn and Fe^{2+} distribution between the M1 and M2 octahedral sites in $MnFeSiO_4$ olivine (Henderson et al., 1996). However, natural spinels are often chemically complex making it impossible to determine site occupancies directly although modelling approaches combining refined **mean** cation-oxygen distances, cell parameters, oxygen coordinates and cation sizes have provided useful data for samples of known chemical composition (e.g., Carbonin *et al*. 1996; Lavina *et al*., 2002; Uchida et al., 2005). Reliable determination of metal oxidation states is even more difficult although iron (^{57}Fe) Mössbauer spectroscopy provides important information on valence, coordination and magnetic ordering (e.g., O'Neill et al., 1992; Carbonin et al., 1996; Doriguetto et al., 2003; Lilova et al., 2012). Below the Curie temperature spectra show complex overlapping peak structures with each distinct Fe environment being represented by a sextet of peaks; above the Curie point each tetrahedral Fe environment shows a single peak while each octahedral environment shows a quadrupole-split double peak. However, for magnetite and other magnetite-rich solid solutions, Mössbauer spectroscopy cannot be used to distinguish the valence state of Fe in octahedral sites as Fe^{3+} and Fe^{2+} are hybridised due to the lifetime of the Fe charged state being too slow (~10^{-8} s.; Wißmann et al. 1998) to freeze electron hopping between Fe^{2+} and Fe^{3+} (timescale ~ 10^{-13} s.; Wißmann et al. 1998).

Many structural studies of spinels have involved room-temperature (room-T) investigations of samples rapidly quenched from high-T; quenching to room-T from 900-1000^{o}C in a few seconds is normally sufficient to freeze in high-T cation occupancies for elements present in a single valence state (e.g., Al, Mg, Ti) but for mixed valence states of Fe, where cation order/disorder may take place simply by electron transfer, it seems that Fe valence equilibration cannot be thermally quenched quantitatively (O'Neill and Navrotsky, 1984; Becker, 2001). Harrison and Putnis (1997b) confirmed that this is also the case for solid solutions with > 70% of magnetite in the system $Fe_3O_4 - MgAl_2O_4$ but that some Fe-valence quenching was possible for more Mg-rich samples. Wu and Mason (1989) carried out high-T thermopower and conductivity measurements on end-member magnetite from 600 to 1600^{o}C in a controlled oxygen atmosphere and deduced equilibrium Fe^{2+} and Fe^{3+} occupancies for the octahedral site based on the assumption that the measurements monitored only electron transfer on that site via a small polaron (hopping) mechanism (timescale ~ 10^{-13} s). Strict magnetite stoichiometry then allowed the occupancies of Fe^{2+} and Fe^{3+} in the tetrahedral site to be allocated.

X-ray absorption spectroscopies (XAS), with a timescale of ~10^{-16} s (Brown et al., 1995) can, in principle, sample the electronic structure faster than the timescale of electron hopping but *K*-edge EXAFS usually only provides **averaged** site information for a given target element; however, the local geometry of the spinel structure allows estimation of its distribution over the tetrahedral and octahedral sites (Henderson et al., 2007). Because *L*-edge XAS probes the empty *d*-orbitals of Fe and because of spin selectivity of X-ray magnetic circular dichroism (XMCD), these latter techniques can easily discriminate between Fe^{2+} and Fe^{3+} as well as provide key information on Td and Oh occupancies for both Fe^{2+} and Fe^{3+} in magnetic phases (see later).

Many studies on synthetic materials have been carried out on samples as close to stoichiometry as possible, but the problem of non-stoichiometry is often difficult to overcome, or even to assess adequately. This is often the case for samples synthesized at high-T (>1000^{O}C) and particularly where the samples contain multivalent 3d transition elements; non-stoichiometry can occur as either a cation deficiency or a cation excess relative to O. Despite this, many models for site occupancy, including that of Nell et al. (1989) for samples in the $MgAl_2O_4 - Fe_3O_4$ solid solution, assume exact magnetite stoichiometry so that Fe^{2+} and Fe^{3+} contents are entirely based on calculation to 4 oxygens and three cations.

Experimental work on the Fe-O system has shown that under oxidising conditions magnetite has cation vacancies with the formula ~$Fe_{2.95}\square_{0.05}O_4$ while under more reducing conditions, it contains excess cations with the formula ~$Fe_{3.002}O_4$ (Dieckmann and Schmalzried 1977a,b); it was assumed that the oxygen sub-lattice is fixed at 4.0 apfu so restricting compositional variation to the cation budget. The structural variations are interpreted as being due to Frenkel-type defects (Dieckmann and Schmalzried, 1977a). Allocation of excess cations to a particular interstitial site is generally difficult for steric reasons as the close proximity of normally-filled and normally-vacant interstitial sites means that filling one leads to a vacancy in the adjacent site.

Navrotsky and Kleppa (1968), O'Neill and Navrotsky (1983, 1984) and O'Neill et al. (1992) made a major contribution to the understanding of spinel group properties by combining structural information and T-dependent Oh-Td site occupancies with enthalpies of formation and calculated electrostatic lattice-energy data to develop a generalised thermodynamic model for cation ordering. O'Neill and Navrotsky (1983) also pointed out the problem of dealing with solid solutions where end-members have different ordering arrangements. This leads to particular problems for the $(Mg\text{-}Fe^{2+})Al_2O_4$ binary where both Mg and Fe^{2+} behave similarly and the end-members are both normal spinels, while in the $(Mg\text{-}Fe^{2+})Fe^{3+}{}_2O_4$ binary Mg and Fe^{2+} again behave similarly but now the end-members are both inverse spinels. Thus, the solid solution series between $MgAl_2O_4$ (normal spinel) and $Fe^{2+}Fe^{3+}{}_2O_4$ (inverse spinel), which is the main topic of this paper, would be expected to show complex structural and thermodynamic properties as far as site occupancies are concerned (Harrison et al.,1999).

EXPERIMENTAL METHODS

Sample preparation, chemical analysis and unit cell edge determination.

Eight synthetic spinel-magnetite solid solutions have been studied in this paper; identifying names have the suffix SP (SPinel). Seven of the samples were first described in Harrison and Putnis (1995): SP3 has the nominal molecular composition 17% Fe_3O_4, others are SP5 (23%); SP9 (40%); SP20 (55%); SP13 (61%); SP17 (71%) and SP14 (81%). The eighth sample, SP50 (51% Fe_3O_4), was first described by Harrison et al. (1999); this sample was originally named NS50. The samples were synthesized at 1400°C and cooled in ~1 sec. by dropping into cold water (Harrison and Putnis, 1995). XRD and TEM study

showed that the samples are single phase although the presence of some diffuse scattering at the base of intense diffraction peaks might suggest short range cation clustering (Harrison and Putnis, 1995).

Energy-dispersive electron microprobe analyses of samples SP 3, SP5 and SP 13 are given in Harrison and Putnis (1995) and those for SP14 and SP17 are from Harrison (1997). Samples SP9, SP 50 (=NS50) and SP 20 were subsequently analysed using a Cameca SX100 wavelength-dispersive microprobe with a 2 micron probe spot at 15 keV, with a 20 nA probe current and with simple oxides, silicates and metals as standards; all matrix corrections were carried out with the Cameca PAP routine.

Unit cell parameters were either taken from Harrison and Putnis (1995) or were determined using CuK_{α} radiation on a Philips PW1060 X-ray diffractometer fitted with a curved-crystal graphite monochromator; each sample was mixed with Si as internal standard. Cell parameters were calculated using the UNITCELL programme of Holland and Redfern (1997). The cation ordering parameters deduced for each element were combined with reliable metal – O bond lengths for each appropriate valence state and cation species and used to calculate mean metal-oxygen bond lengths for the tetrahedral (A–O) and octahedral (B – O) sites. The mean bond lengths were then used to calculate the unit cell edge (a) and oxygen parameter *(u)* based on the following equations (Hill et al., 1979; , O'Neill and Navrotsky, 1983; Lavina et al., 2002; Henderson et al., 2007):

$$a = (8/11\sqrt{3})\,[5(A - O) + \sqrt{(33(B - O)^2 - 8(A - O)^2}] \quad \text{..... (1)}$$

$$u = (0.75R - 2 + \sqrt{(33R/16 - 0.5)})/[6(R - 1)] \quad \text{where } R = (B - O)^2/(A - O)^{2-} \text{.... (2)}$$

XAS Measurements

Fe and Mg K-edge XAS. All XANES and EXAFS K-edge data were collected at the CLRC Daresbury SRS, operating at 2 GeV with an average current of 150 mA. For the Mg K-edges the samples were ground with boron nitride and pressed into flat disks. Data were collected *in vacuo* on the soft X-ray station 3.4 with a pair of beryl (100) monochromating crystals with spectra measured in total electron yield (TEY) mode. Spectra at the Fe K-edge were collected in transmission on station 8.1, using a double crystal Si(220) monochomator detuned to 50% transmission with the samples mounted in aluminium sample

holders with Sellotape windows and diluted with boron nitride to optimize the edge jump. Energy scales were calibrated using MgO and Fe foil.

Background subtracted EXAFS spectra were analysed in EXCURV98 (Binsted, 1998; Gurman et al., 1984) to obtain first shell bond distances and estimates for the proportions of bulk Fe in each structural site (see Henderson *et al*. (2007) for further details). The same approach was used to obtain similar data for Mg but the short *k*-range, due to the Al K-edge ~256 eV above the Mg K-edge, limits the quality of the estimates.

Fe $L_{2,3}$ XAS and XMCD. The synthetic spinel-magnetite solid solutions were measured at room-T on beamline 4.0.2 at the Advanced Light Source (ALS) in Berkeley, California, using the eight-pole resistive magnet endstation (Arenholz and Prestemon, 2005). The XAS signal of freshly ground powder was monitored in TEY mode. At each photon energy point of the spectrum, the X-ray absorption was measured for two opposite magnetisation directions by reversing the applied magnetic field (0.6 Tesla). The XAS signals for each magnetization direction were normalized to the incident beam and subtracted to give the XMCD spectrum (Pattrick et al., 2002). To calibrate the energy scale a standard magnetite, which had been calibrated against metallic Fe, was run with each batch of samples. Note that van der Laan and Figueroa (2014) give an excellent review of this technique

At room-T the five most Fe-rich samples are ferrimagnetic with Curie temperatures (Harrison and Putnis, 1995, 1996) in the range 380 – 710 K (Table 1) while the three most Mg-rich samples have low Curie temperatures (Table 1) and are paramagnetic at room-T in the absence of an external magnetic field. Thus for the paramagnetic samples the weak XMCD signal at room T results from the reversal of the paramagnetic moment in the 0.6 Tesla applied magnetic field. For the latter samples, XMCD spectra were also measured at 20 K which is below the Curie temperature for sample SP9 (215K; Harrison and Putnis, 1996) but the data at 20 K for samples SP3 and SP5 were too noisy to be fitted reliably. For all the samples average Fe *L*-edge XAS spectra were obtained by summing the signals for the two magnetization directions.

The spectral resolution for the XMCD data is sufficient to attempt to fit four peaks in the Fe-L_3 region with positive, negative, positive, negative signals equivalent to crystallographic sites for Fe d^6T_d (at ~ 709 eV); Fe d^6O_h (~710 eV); Fe $d^5\,T_d$ (~711 eV); and Fe $d^5\,O_h$ (~712 eV), respectively. To obtain the

222 cation distribution over the four Fe sites, the experimental XMCD spectra were fitted by means of a
223 nonlinear least-squares analysis, using the calculated spectra for each site (van der Laan and Thole, 1991;
224 van der Laan and Kirkman,1992); the 10Dq crystal field parameters were taken as 1.4 eV for Fe O_h sites
225 and -1.0 eV and -0.7 eV for Fe d^6T_d and d^5T_d respectively. Further experimental and spectrum fitting
226 details can be seen in Pearce et al. (2010). For the Fe-rich samples relative errors are likely to be ~ ± 2% for
227 the site occupancies (Pearce et al., 2010), however, the Mg-rich samples have larger errors (5-10%) because
228 of the lower Fe contents and weaker magnetic signals.

229 Several papers have addressed the inter-relationships between primary-beam penetration depth (i.e.,
230 attenuation length, $\lambda\cos\theta$ where θ is the angle of incidence) and electron escape depth (λ_e) and the
231 implications to surface sensitivity and spectral saturation (e.g., Nakajima et al., 1999; Goering et al., 2006;
232 van der Laan and Figueroa, 2014). Saturation is less likely to be a factor when the attenuation length is
233 significantly greater than the escape depth. It is well known that the TEY detection technique is surface
234 sensitive with λ_e typically in the range 3-5 nm for the $L_{2,3}$ edges of 3d transition elements (van der Laan and
235 Figueroa, 2014) which makes it an ideal tool in soft-X-ray absorption spectroscopy for analysing thin films,
236 nano-samples and samples with thin surface layers. However, λ_e is dependent on sample-type and
237 composition; Gota et al. (2000) provide a value of 4.5 nm for an epitaxially grown film of Fe_3O_4 with a
238 penetration depth of ~170 Å for Fe L_3.

239 Our XMCD experiments were carried out on freshly crushed powders using TEY detection and,
240 while the surface topology is different, the penetration and escape depths for the $L_{2,3}$ are similar to those
241 reported above. The Fe *L*-edge data probe the surface compositions of the samples but, if the sample grains
242 are chemically and structurally homogenous, such surface sensitivity does not present a problem. The
243 exposure of fresh surfaces limits any potential for surface oxidation and surface stoichiometries that match
244 those for the bulk have previously been measured using this technique (Pearce et al., 2010). In addition,
245 note that our XMCD relative peak areas are recalculated to the analysed elemental Fe content so that it is
246 not necessary to apply a saturation correction to the Fe L-edge data. Our Mg K-edge XAS experiments
247 were also carried out on powders with TEY detection but the ~1.3 keV beam energy, based on
248 photoabsorption cross section differences, would have had a greater penetration depth (~1 μm) and a
249 proportionately larger escape depth of ~10 μm.

It is useful to combine results from soft-X-ray TEY results for powdered samples with data from more penetrating techniques. Thus, Fe *K*-edge XANES and EXAFS data of 'bulk' samples (10 micron length scale) complement *L*-edge studies of the same samples (e.g., Lilova et al., 2012 and this work). The reliability of our XMCD surface-based analyses for capturing bulk sample characteristics is confirmed by comparing calculated unit cell edges and calculated magnetic moments to values measured on bulk powder samples.

RESULTS AND INTERPRETATION

Chemical analyses

Electron microprobe analysis averages (wt.%) are given in Table 1 along with 1 sigma standard deviations. Atomic formulae data were recalculated assuming ideal stoichiometry (4 oxygens and 3 cations; Droop, 1987) and these data, including 'model' Fe^{3+} and Fe^{2+} values, are also shown in Table 1. As would be expected for this method of calculation the $Fe^{3+}/(Fe^{2+}+Fe^{3+})$ atomic ratio is close to the ideal value of 0.66 except for the two most magnesian samples SP3 and SP5 which both appear to be displaced towards non-stoichiometry involving some w□stite component (Table 1). Measured unit cell edges (Harrison and Putnis, 1995), estimated errors, and Curie temperatures (Harrison and Putnis, 1996) are also shown.

K-edge XANES and EXAFS data for Mg and Fe.

Near-edge (XANES) spectral features provide radial structural information to about 20 Å from the target element while refinement of the EXAFS gives bond distances and ligand coordination information normally to < 6 Å. Ildefonse et al. (1995) found that the first prominent XANES peak for 4-coordinated Mg in $MgAl_2O_4$ occurs at ~ 1309 eV while that for 6-fold Mg in MgO is higher at ~ 1310 - 1311 eV. For other model compounds with 6-coordinated Mg (e.g., montmorillonite and cordierite; Li et al., 1999; Trcera et al., 2009) this feature is much weaker and only occurs as a shoulder on higher energy peaks. Thus a distinct peak at 1309 eV is diagnostic for Mg in tetrahedral coordination. Figure 1 shows Mg K-edge XANES spectra for five of the solid solutions plus that for end-member $MgAl_2O_4$ and the peak at 1309 eV becomes progressively smaller as Mg decreases. We conclude that tetrahedral Mg is a major component in

276 the spinels with 25% (SP5) and 40% (SP9) Fe_3O_4 in solid solution but decreases progressively and is only a
277 minor component in the sample with 80% Fe_3O_4 (SP14). With decreasing Mg content a small peak at
278 ~1313-1314 eV increases in height progressively and the overall XANES features become more like those
279 for 6-coordinated Mg in talc (Li et al., 1999).

280 Fe-K-edge XANES spectra are shown in Figure 2 and exhibit only small (although significant)
281 differences with changing composition. Thus the edge crest feature at ~7132 eV becomes slightly better
282 defined as Fe decreases, while sample SP5 (Fig.2) shows a small change in slope on the edge at ~7120 eV
283 and a small bulge on the low energy side of the pre-edge peak at ~7112 eV. Berry et al. (2003) have shown
284 that the features at 7113 and 7120 eV are more pronounced for more reduced compositions and thus sample
285 SP5 may be more reduced than a stoichiometric composition.

286 Data obtained from refining the *K*-edge EXAFS spectra for Fe and Mg are summarized in Table 2.
287 The Fe *K*-edge energy is significantly lower for the two Mg-rich samples confirming that the Fe is more
288 reduced than in the other samples (see above). The pre-edge height shows no significant variation and its
289 intensity is consistent with a mixture of Fe oxidation over the two cation sites. The refined tetrahedral Fe –
290 O bond lengths are ~ 1.84 Å; this anomalously small value is consistent with the presence of Fe^{3+} in a
291 distorted site (*cf.* Eisenberger and Brown, 1979). The octahedral Fe – O is also anomalously small
292 consistent with the Fe occurring in distorted sites (see Henderson et al., 2007). The estimated data for the
293 occupancies of Fe over the two sites are also given in Table 2 as % of total Fe in each site. Henderson et al.
294 (2007) found that the tetrahedral occupancies measured for a range of 3*d* elements in spinel were about 10-
295 20% higher than expected for stoichiometric samples; the values reported in Table 2 for the present samples
296 have therefore been reduced on average by 15% (relative). The occupancy for Fe decreases from ~45% to
297 ~35% (Fe^{3+} 0.32 – 0.85 apfu) with increasing magnetite content (denoted Mgt). The occupancies for Mg_{Td}
298 decrease from ~54% to ~42% (Mg 0.41 – 0.09 apfu) with increasing Mgt.

299 These occupancy estimates are combined with atomic formulae data for Fe and Mg and are
300 reported as normalised occupancy data for each of the two cation sites (Table 2). We have tentatively used
301 these data to estimate the Al occupancies (atoms Al pfu) assuming cation totals of 1.000 and 2.000 for
302 tetrahedral and octahedral sites (Table 2). We do not claim a high accuracy for the EXAFS data but are
303 confident that trends over the series are reliable.

Fe $L_{2,3}$ X-ray absorption spectroscopy (XAS).

Figure 3 shows Fe $L_{2,3}$-edge XAS spectra for all of the solid solutions studied; this type of spectroscopy probes the local electronic structure and provides information on Fe oxidation state and site-symmetry (van der Laan and Kirkman, 1992). The main peak for the most magnetite-rich sample (SP14) is very similar to that for end-member natural magnetite (Figure 2 in Pearce et al., 2006) in that only a weak shoulder is present on the low energy side of the main peak; this feature is considered to be typical of end-member magnetite which lacks any significant oxidation towards a phase containing the maghemite molecule (Zhu et al., 2015; see also Fig. 3 in Graf et al., 2015). With increasing Mg-content the XAS spectra show that the feature on the low energy side of the main L_3 peak becomes progressively better resolved and more intense; note that the spectrum for the Mg-rich sample SP5 is similar to that for a natural magnesian spinel ($Mgt_{0.20}$, BM1983,595) (Cressey et al.,1993; Henderson et al., 1996). Although samples in the compositional range Mgt_{51-100} (SP50 to natural magnetite) show differences in peak resolution, the energy differences between the main peak and the lower energy feature show no significant change ~ 1.25 – 1.16 eV (i.e. 1.21 ± 0.04 eV). For the two most Mg-rich synthetic samples (SP3 and SP5) and the natural magnesian spinel (Cressey et al., 1993) the Fe $L_{2,3}$ -edge peaks have a larger energy separation (1.64-1.71 eV; 1.68 ± 0.03 eV) than for the Fe-rich samples. This separation is similar to that (~ 1.6 eV) between reduced (lower energy peak) and oxidised Fe in an $L_{2,3}$ spectroscopy study of zoned oxidised magnetites (Gilbert et al., 2010) and in reduced and oxidised versions of organic dinuclear Fe-oxo compounds (Peng et al., 1995) . Sample SP9 shows intermediate properties with a peak separation of ~1.45 eV. We conclude that the more-pronounced lower energy peaks in Mg-rich samples SP3 and SP5 reflect the presence of a greater proportion of Fe^{2+} than expected from the nominal spinel-magnetite stoichiometry and this is confirmed by the Fe K-edge data (see above). Note that the red spectra in Figure 3 show the actual XMCD intensities for each sample and demonstrate the relative weaknesses of the XMCD signals in samples SP3 and SP5 which have the lowest Fe contents (see later).

It is clear that the bonding features for Fe over the composition range Mgt_{100-51} are very similar despite the large range of composition and we speculate that these solid solutions might show a degree of Fe clustering with short-range structure similar to that in end-member magnetite. By contrast, the most Mg-rich solid solutions show very different electronic structures perhaps due to the Fe, Mg and Al cations

being more homogeneously distributed. Sample SP9 appears to show a more mixed bonding structure; we will return to this point later.

Fe $L_{2,3}$ XMCD spectra.

Figure 4 shows the XMCD spectra obtained at room-T and the best fits to the four possible Fe L_3 peaks. Note that the y axis scales show that the intensity of the magnetic signals reflect the absolute Fe contents of the solid solutions except that the intensities of the three most magnesian samples are proportionately much smaller than those for the Fe-rich samples; i.e. SP9 ($Mgt_{0.41}$) has ½ the Fe content of SP14 ($Mgt_{0.81}$) but the peaks are 5 times smaller. This relationship is shown in Figure 5 where the combined XMCD peak heights for the different species are plotted against bulk composition. These differences are related to the fact that at room-T the three most magnesian samples are paramagnetic while all the other samples are ferrimagnetic. Indeed, XMCD spectra for the paramagnetic samples can only be obtained because the electron spins become aligned in the 0.6 Tesla applied magnetic field. However, we have recently obtained XMCD data at 20K for samples SP9, SP5 and SP3; this temperature is below the Curie temperature for SP9 and gave a much higher XMCD signal for the ferrimagnetic species compared to that for the room-T paramagnetic version as shown in Figure 5. The 20K data for SP3 and SP5 are very noisy and could not be refined to assess any XMCD signal; it is likely that the Curie-T for both of these samples is lower than 20K.

The lower part of Table 1 contains values for the bulk Fe^{2+} and Fe^{3+} concentrations determined from the XMCD spectra based on cell formulae calculated to 4 oxygens, together with the equivalent cation proportions for Al, Mg and the minor Si content present. Note that estimated errors for the different atomic species are shown. The cation sums show an excess over 3.0 (range 3.000 – 3.067, Table 1) and all the element cation numbers are slightly higher than those calculated to 4 oxygens and 3 cations (upper part of Table 1). The XMCD Fe^{3+}/total Fe ratios (Table 1) for the two most Mg-rich solid solutions are similar to that reported for a natural Mg-rich spinel (Cressey et al., 1993) and are significantly lower than the 'stoichiometric' ratio of 0.66 (cf. Fe absorption edge energy values, Table 2); the other samples also show some departures from this value ranging 0.582 to 0.694. Thus, while conventional recalculation of spinel analyses to the ideal 4 oxygens and 3 cations appears to show that synthetic and natural spinels are

359 generally stoichiometric, the measurement of actual Fe oxidation states suggests that samples may not
360 follow a strict magnetite stoichiometry (*cf.* Pearce et al., 2006).

361 The energy resolution of XMCD spectra for these samples is sufficiently high to allow the presence
362 of small amounts of Fe^{2+} in Td sites to be estimated over the solid solution range from Mgt_{40} to Mgt_{70} but
363 this spectral component does not occur for the most Fe-rich samples (Table 3). The fact that Fe^{2+}_{Td} cannot
364 be detected in sample SP14 (Mgt_{81}) is consistent with its absence in end-member magnetite (e.g., Kuiper et
365 al., 1997; Pattrick et al.. 2002; Pearce et al., 2010). The apparent absence of Fe^{2+}_{Td} for the two most Mg-
366 rich samples is likely to reflect the higher errors involved with fitting the weak paramagnetic signals for
367 these samples. The Fe-occupied sites in these samples are more likely to have Mg or Al in adjacent sites
368 thus more strongly localised Fe electronic states can be expected, resulting in the observed increased energy
369 separation between the Fe^{2+} and Fe^{3+} spectral features in the L_3 edge (see earlier). The parameters used to fit
370 the different Fe structural environments might thus be less reliable than for the Fe-rich samples on which
371 they are based. Figures 6a and 6b show the variation in Fe cation occupancies for the room-T data *versus*
372 magnetite content in Td and Oh, respectively. The site occupancy values for SP9 at 20K fit the
373 compositional trends better than the room-T values but are not shown in Figure 6 as all the other sample
374 data in this figure are for the same temperature (298 K). The striking feature is that the trend for Fe^{3+}_{Td}
375 (Figure 6a) is close to a linear fit ($Fe^{3+}_{Td} = 1.047 \times Mgt_x$; R^2 0.988) pointing to the strong tetrahedral site
376 preference shown by Fe^{3+} in magnetite-bearing spinels (Goodenough and Loeb, 1955; Pattrick et al., 2002)
377 at room-T. The Fe^{2+}_{Oh} occupancies (Figure 6b) are slightly scattered about a 1:1 trend with the two most
378 Mg-rich and the two most Fe-rich solid solutions showing a small excess of Fe^{2+}_{Oh} over that expected for a
379 stoichiometric magnetite-bearing solid solution; this is consistent with four of our samples having small
380 amounts of wüstite (FeO) in solid solution (*cf.* Dieckmann and Schmalzried, 1977b). The presence of
381 minor Fe^{2+}_{Td} in the middle of the solid solution series defines a distinct shallow hump in Figure 6a while
382 that for Fe^{3+}_{Oh} falls below that for an idealized 1:1 magnetite-like trend, especially for the more Fe-rich
383 members of the intermediate solid solutions (Figure 6b).

384 It is clear that the Fe^{3+}_{Td} trend for the solid solutions falls very close to the join between end-
385 member spinel and end-member magnetite which is fully ordered (inverse) at room-T (Figure 6a). The very
386 low or zero Fe^{2+}_{Td} occupancies for the Fe-rich solid solutions also points to an inverse magnetite-like

structure for these samples at room-T. It seems that rapid quenching of the Fe-rich samples did not prevent the rapid equilibration of Fe^{2+} and Fe^{3+} by electron transfer as predicted by Wu and Mason (1981), O'Neill and Navrotsky (1984) and Becker (2001). The Fe^{2+}_{Oh} and Fe^{3+}_{Oh} site occupancies show a similar magnetite-like trend down to about $Mgt_{0.55}$ indicating rapid electron transfer on the octahedral site but the relatively high Fe^{2+}_{Td} values for SP9 and SP50 suggest that the tetrahedral Fe oxidation ratio might have been quenched-in below about 500-600^{o}C. By contrast the more Fe-rich samples show decreasing Fe^{2+}_{Td} values consistent with a greater degree of electron transfer with increasing Fe_3O_4 in solid solution. It seems that increasing amounts of Mg and Al in solid solution reduce the efficiency of electron transfer between Fe ions on the different cation sites.

Site occupancy determination.

While our XMCD data provide values for the occupancies of Fe^{2+} and Fe^{3+} in tetrahedral and octahedral sites it is necessary to allocate Al, Mg and Si to these sites. It is well known that Al in spinels is strongly partitioned into Oh sites and we have set up occupancy models based on the tetrahedral sites containing 10% total Al with the rest in Oh; this value is chosen to match the values determined for Al by *K*-edge EXAFS (Henderson, 2007), by analyses and structural work on natural spinels (e.g.,Waerenborgh et al., 1994; Nakatsuka et al., 2004), and on high-T NMR experiments at 800^{o} to 1000^{o}C (Harrison et al., 1998; Redfern et al., 1999; Martignago et al., 2006) which represents the likely quenched-in Al configuration.

These values are combined with the determined XMCD Fe^{2+} and Fe^{3+} occupancies while the small Si content is allocated to the Td site as advocated for Si-rich magnetites (Huberty et al., 2012). In such spinels, any cation excess or deficiency is likely to be associated with the octahedral sites, so the tetrahedral site is now made up to a total of 1.000 cations with Mg. The remaining Mg is allocated to Oh along with the measured Fe^{2+}_{Oh} and Fe^{3+}_{Oh} and residual Al. Table 3 gives the site occupancy data for this model. It is not a simple matter to establish where excess cations might be located but it is likely that they would occupy 'normally vacant' interstitial sites with implications to the probability of a cation occurring in an adjacent 'normally occupied' lattice site i.e., a Frenkel defect mechanism.

The site occupancies for Fe^{2+} and Fe^{3+} obtained by XMCD clearly refer to the outer 3-5 nm of the powders studied. We have shown that the Fe-rich samples show no signs of an oxidised surface, indeed

415 both Fe $L_{2,3}$ XAS spectra and the deeper-probing Fe K-edge XANES confirm the evidence that the most Mg
416 rich samples have excess Fe^{2+} rather than excess Fe^{3+}. We conclude that there is no evidence that the bulk
417 of our samples have been affected by oxidation since their initial synthesis. We can test the reliability of
418 this conclusion by using the determined site occupancy data (Table 3) to calculate the mean A-O and B-O
419 bond lengths and then the cubic unit cell edges (a) and oxygen (u) parameters using equations (1) – (2)
420 (section Experimental Methods section). Measured unit cell edges for the samples clearly refer to their bulk
421 structure and composition and comparison of these to the a values determined here should establish whether
422 or not the surface data represent a reliable probe for the sample as a whole.
423 In order to calculate the a values it is necessary to utilise average sizes for both tetrahedrally and
424 octahedrally coordinated cations, together with the associated vacancies, irrespective of whether they are
425 present in 'normal' or 'interstitial' sites. The adopted M – O values used are the same as those in
426 Henderson et al. (2007) except that a value of 1.885Å for $(Fe^{3+} - O)_A$ was found to be more reliable across
427 the whole solid solution series; in addition a value for $(Fe^{2+}\text{-}O)_A$ of 2.01 Å was adopted (Shannon, 1976). In
428 the first instance we used estimates of 2.0 Å for a tetrahedral vacancy and 2.11 Å for an octahedral vacancy
429 (Lavina et al., 2002); however, detailed calculations for these samples and oxidised titanomagnetites and
430 maghemite (work in progress) suggest that more reliable estimates are 2.05 Å and 2.12 Å.
431 Calculated unit cell edges are given in Table 3; based on analytical errors for individual atom
432 species it is likely that the cell-edge error is ~ 0.005 Å across the solid solution series. Note that errors
433 greater than ~ 0.03 atoms pfu for the distribution between A and B sites or in Fe^{2+}:Fe^{3+} would lead to a
434 values significantly higher or lower than the values found here. The model with 10% total Al in Td matches
435 the measured cell edges and published structures for pure $MgAl_2O_4$ (Yamanaka and Takeuchi, 1983). For
436 our synthetic solid solutions the calculated and measured cell edge values show excellent agreement (see
437 bold figures in Table 3) with agreement for most samples being better than 0.005 Å and only two (SP9 for
438 298 K data and SP50) showing a mismatch > 0.01 Å. However, the better defined data for SP9 at 20K gives
439 a cell edge very close to the measured value. The Mg occupancies in Td calculated for the model with 10%
440 total Al vary from 47 to 85% of total Mg with increasing Mg content. Published assignments for Mg tend
441 to range ~40 to 85% (Carbonin et al., 1996; Nakatsuka et al., 2004; Henderson et al., 2007) in excellent
442 agreement with our adopted site occupancies. Finally, the decrease in the Mg-site occupancies with

443 increasing Mgt content, and the scale of Al entry into the tetrahedral site (Table 2), are broadly in line with
444 the above suggestions. Taking account of the trends across the solid solution series we conclude that the
445 data in Table 3 provide reliable site assignments, show that the surface composition of our samples is
446 essentially the same as the bulk, and define a robust basis for rationalising the structures of the $MgAl_2O_4$ –
447 Fe_3O_4 spinel series. Based on the trivalent cation occupancies determined for the tetrahedral site the
448 transition from 'more-normal' to 'more-inverse' spinel (i.e. $(Al+Fe^{3+})_{Td} = 0.5$) appears to occur at ~$Mgt_{0.36}$.

449 Our adopted site occupancy data for Al and Mg in tetrahedral and octahedral sites are displayed in
450 Figures 6a and 6b as a function of magnetite content. The Al trends, of course, are fixed to be a linear trend
451 with 10% of total Al occurring in A and 90% in B. The Mg data show a pronounced affinity for the
452 tetrahedral site for the most Mg-rich bulk compositions and this affinity decreases as Mgt increases until
453 Mg shows equal entry into tetrahedral and octahedral sites over the range $Mgt_{0.5\text{-}1.0}$. The tendency for Mg_{Td}
454 to be larger for Mg-rich spinels than for Fe-rich members of this solid solution is in line with the EXAFS
455 data of Henderson et al. (2007) which gives a tetrahedral site occupancy (Mg_{Td}/total Mg) of 0.79 for
456 $MgAl_2O_4$ and an average of 0.44 ± 0.12 for five synthetic Fe-rich Fe-Mg-Ni-Co-Al-bearing spinels.

457 **DISCUSSION**

458 In this paper we have established the presence of non-stoichiometry involving cation excesses (cation
459 totals > 3.0 pfu) which seem to occur in octahedral interstitial sites. No tetrahedral Fe^{2+} is detected in the
460 Fe-rich and the Mg-rich samples and only small amounts in the intermediate members. By contrast,
461 reduced Fe (hercynite-rich), and high-Al and -Cr spinels contain abundant Fe^{2+} in the A site (e.g., Della
462 Giusta et al.,1996; Uchida et al., 2005) and Andreozzi and Lucchesi (2002) found that synthetic solid
463 solutions in the system $MgAl_2O_4$ - $FeAl_2O_4$ (hercynite) showed a marked preference for Fe^{2+} over Mg in the
464 tetrahedral site. In addition, Palin and Harrison (2007) used Monte Carlo computer modelling for this
465 system to show that Fe^{2+} has a small tetrahedral preference for Td compared to Mg. The situation is
466 different for our more oxidised spinel – magnetite series and it seems that repulsive interactions between
467 Fe^{2+} or Mg and Al or Fe^{3+} are very different and play a crucial role in controlling cation site preferences in
468 spinels.

469 It is likely that our quenched samples retained disordered arrangements for Mg and Al typical of
470 equilibrium partitioning at ~ 800 – 1000 ^{o}C and that Fe^{2+} and Fe^{3+} atoms did not diffuse between Td and Oh

sites during quenching. However, electron exchange reactions between Fe^{2+} and Fe^{3+} in adjacent sites are much too fast to freeze-in quantitatively during the quench. Fe-rich members in the solid solutions will have a higher probability of adjacent sites containing a pair of Fe ions of the correct valence to allow the electron exchange, while Fe-poor members of the solid solution would be more likely to have Mg or Al as nearest neighbours to an Fe site and this would limit the probability of electron transfer (*cf.* Verwey et al., 1947). The presence of higher Fe^{2+}_{Td} in intermediate solid solutions compared to those in more Fe-rich samples reflects this relationship. Indeed, this is the same situation found with Mössbauer spectroscopy of Fe-poor spinel solid solutions where B-site Fe^{2+} and Fe^{3+} are not hybridised and produce separate sets of spectral lines (Bahgat et al., 1980).

It is generally agreed that at room-T Fe^{2+} and Fe^{3+} atoms in the octahedral site are hybridised due to an electron (small polaron) hopping between adjacent sites. However, Verwey et al. (1947) pointed out that while electron interchange between Fe^{2+} and Fe^{3+} in adjacent octahedral sites was particularly favourable there was also the possibility of exchange either between Fe^{2+} and Fe^{3+} in adjacent A - A sites or between adjacent A - B sites. Dieckmann et al. (1983) concluded that high-T thermopower measurements for magnetite were consistent with electron transfer by all three mechanisms. In addition, Wißmann et al. (1998) studied magnetite using high-T Mössbauer spectroscopy and found very fast hopping of electrons between Fe^{2+} and Fe^{3+} in adjacent B sites (timescale 10^{-13} s); electron hopping between adjacent A sites was considered to be only slightly slower (10^{-12} s). Our XMCD results are consistent with very rapid Fe valency equilibration having occurred between Fe^{2+} and Fe^{3+} on both structural sites during the fast quenching. In any case, the presence of delocalised electrons at low temperatures might be expected as magnetite is considered to have semi-metal properties under these conditions (e.g., Parker and Tinsley, 1976; Schedin et al., 2004).

Nell et al. (1989) and Nell and Wood (1989) carried out important *in situ* thermopower measurements on four synthetic $MgAl_2O_4$ – Fe_3O_4 samples ($Mgt_{0.25}$, $Mgt_{0.50}$, $Mgt_{0.75}$, and $Mgt_{1.00}$) as a function of temperature. Fe^{2+} and Fe^{3+} site occupancies in both tetrahedral and octahedral sites were deduced from these measurements using the approach of Wu and Mason (1981). An estimate of the Al content in the tetrahedral site was obtained using the model of O'Neill and Navrotsky (1983); the other occupancy data were then obtained from the sample bulk compositions assuming exact spinel

499 stoichiometry. Nell et al. (1989) displayed the compositional dependence of site occupancies at 1000°C
500 (their figure 9) compared with values calculated using the O'Neill - Navrotsky model. Nell et al. (1989)
501 considered that measurements and the calculated model data were in reasonable agreement, however, Mg_{Td}
502 is close to zero for the two more Fe-rich solid solutions, and Fe^{2+}_{Oh} and Fe^{3+}_{Oh} are surprisingly small for the
503 Mg-rich solid solution.

504 Nell and Wood (1989) subsequently refitted the experimental data and the new occupancy data
505 were figured for 1000°C (their figure 4) together with new model curves and these show generally good
506 agreement. The two Fe-rich solid solutions now have more sensible values for Mg_{Td} but the Al_{Td} is
507 anomalously small. The Fe_{Oh} in the most Mg-rich sample is also still anomalously small (see above). The
508 thermopower measurements for the latter sample could not be reversed which Nell et al. (1989) attributed to
509 a disequilibrium order-disorder phenomenon. However, we suggest that this problem might be related to
510 abundant Al and Mg reducing the probability of having the appropriate Fe ions in nearest-neighbour
511 octahedral sites. This in turn would reduce the probability of the electron transfer and thus the reliability of
512 the $(Fe^{2+}/Fe^{3+})_{Oh}$ estimation. The activation energy of electron hopping in their $Mgt_{0.25}$ sample is almost
513 double that for their $Mgt_{0.75}$ sample (Nell et al., 1989; their figure 4) consistent with this suggestion.

514 Further insight comes from high-T neutron powder diffraction studies for three synthetic samples
515 from the spinel – magnetite system (samples NS75 ($Mgt_{0.25}$), NS50 (Mgt_{50}, our SP50), NS40 (Mgt_{60})
516 (Harrison and Putnis, 1997b; Harrison et al., 1999). Cation site occupancies deduced from diffraction data
517 and saturation magnetism measurements (M_s) showed crucial differences to those predicted by the O'Neill-
518 Navrotsky model; in particular the experimental data showed that Fe^{3+} orders onto tetrahedral sites which is
519 the opposite to predictions based on thermodynamic models. The experimental partitioning results show the
520 same types of mismatch when compared to the Nell and Wood (1989) thermodynamic model. Thus,
521 Harrison et al. (1999) proposed new ordering schemes including a 'pseudo-random model' in which Al
522 occupancies were fixed and then Mg, Fe^{2+}, and Fe^{3+} were randomly distributed over the Td and Oh sites;
523 note that the Fe^{2+} and Fe^{3+} values were those obtained assuming exact stoichiometry.

524 The site occupancies determined by Nell and Wood (1989) and for the pseudo-random model of
525 Harrison et al. (1999) for a temperature of 1000°C can be compared in Table 4; also given (columns G, H
526 and I) are our XMCD-based data for the equivalent samples at 25 °C. Although we have used different

logic to that of Harrison et al. (1999) we find similar values for Mg and Al occupancies in both Td and Oh sites for all three samples (Table 4, compare column D with G, E with H, F with I). However, our data for Fe occupancies are different because we find only small room-T Fe^{2+}_{Td} values for each sample. The site occupancies show clear differences between the data from Nell et al. (1989) and Nell and Wood (1989) and the data for both the Mgt_{50} (SP50) and Mg_{25} (SP5) samples (Harrison et al., 1999 and this paper). Similar mismatches occur when Nell and Wood's data for $Mgt_{0.75}$ (Table 4 column A) are compared with those for $Mgt_{0.60}$ (columns D and G). Harrison et al. (1999) and our data show significantly larger values for Mg_{Td} and Al_{Td} than those adopted in Nell's work which means that Nell allocated much more Fe to Td and therefore less to Oh. This results in very different values for the calculated saturation magnetization (see Tables 3 and 4) where M_s is simply the difference between the Fe content of the octahedral and tetrahedral sublattices if their electron spin alignments are assumed to be exactly anti-parallel (Néel, 1955):

$$M_s = 2[\mu_{Fe3+}X^{oct}_{Fe3+} + \mu_{Fe2+}X^{oct}_{Fe2+}] - [\mu_{Fe3+}X^{tet}_{Fe3+} + \mu_{Fe2+}X^{tet}_{Fe2+}]$$

where μ_{Fe3+} and μ_{Fe2+} have values of 5 μ_B for Fe^{3+} and 4.06 μ_B for Fe^{2+} (μ_B is the Bohr magneton). Clearly a larger proportion of total Fe in the octahedral site will have more effect on increasing the magnetic moment than a larger proportion of Fe^{3+} compared to Fe^{2+} in either site. Thus, for a given composition solid solution (e.g., Mgt_{50}) the higher Fe content in the tetrahedral site reported by Nell and Wood (1989) is responsible for the much lower calculated M_s which has negative values for their more magnesian samples (Table 4 columns B and C). Even though our XMCD measurements at room-T for the quenched sample do not reflect the high-T Fe^{2+}_{Td}, and thus the measured Fe^{3+}_{Oh} is too low, the calculated M_s values for our samples $Mgt_{0.60}$ and $Mgt_{0.50}$ are very similar to those calculated for the high-T Fe valence configuration deduced by Harrison et al. (1999) (Table 4, compare columns D and G, and E and H). Note that we find a higher Mg_{Td} content for the $Mgt_{0.25}$ sample compared to that of Harrison et al. (1999) and this leads to an even higher calculated M_s value (Table 4, compare columns F and I).

We have attempted to model high-T Fe^{2+} and Fe^{3+} contents for our samples based on the pseudo-random model of Harrison et al. (1999) and Harrison and Putnis (1999) where Al_{Oh}:Al_{Td} occupancy is fixed at 90%:10% total Al followed by random distribution of bulk Fe^{2+}, Fe^{3+} and Mg over both sites. The site occupancies for the three samples discussed so far are given in Table 4, columns J, K and L and are displayed in Figure 7 for all samples. The data for end-member spinel are fixed by our earlier assumption

555 on Al occupancy while for end-member magnetite the totally disordered occupancies of 0.666 for Fe^{3+}_{Td}
556 and Fe^{2+}_{Oh}, 1.333 for Fe^{3+}_{Oh}, and 0.333 for Fe^{2+}_{Td} are adopted (Figure 7). Such a fully disordered state
557 would refer to high temperatures, perhaps above 1200^{O}C (*cf.* Wu and Mason, 1981;Wißmann et al., 1998).
558 In Figure 7, the occupancy data for the intermediate solid solutions fall on fairly smooth curves
559 between the two end members; this would be expected for a continuous solid solution series without a
560 phase transition or intermediate compound. Our calculated pseudo-random model M_s values for the Fe-rich
561 samples ($Mgt_{0.61}$ and $Mgt_{0.50}$) show good agreement with the measured magnetic properties and the
562 calculated values from Harrison et al. (1999); in Table 4 compare column J with D and G and column K
563 with E and H. However, the negative M_s value for $Mgt_{0.25}$ (Table 4, column L) is much smaller than our
564 other M_s values reported in Table 4 for this composition (e.g., 1.17 for the XMCD model at 25^{o}C). The
565 same is also true for our sample $Mgt_{0.17}$ (SP3) which gives an M_s of -0.56 for the pseudo-random model
566 compared to a value of 1.00 for the XMCD model at 25^{o}C.
567 These very small M_s values for the two Mg-rich samples are due to this model having much
568 smaller Mg_{Td} occupancies than those determined for the XMCD model (compare Figures 6 and 7) resulting
569 in an associated higher tetrahedral Fe. We believe that our Mg assignments for the XMCD model at 25^{o}C
570 are reliable as they are supported by direct measurement of Fe^{3+} and Fe^{2+} in Td and on EXAFS
571 measurements for Mg site distribution. The bulk composition is fixed so the bulk Fe^{2+} and Fe^{3+}
572 concentrations are fixed, it is only their distributions over the two sites that vary as a result of the electron
573 transfer interactions. We have therefore set up a 'high-T' model for our samples based on the Al and Mg
574 occupancy data for our XMCD model (*cf.* Table 4, columns M, N and O with G, H and I). The Mg_{Td} for
575 all the samples are larger than those for the pseudo-random model but the Mg-rich samples have
576 particularly high values (compare Table 4 columns L and O). We pointed out earlier that the intermediate
577 members of a continuous solid solution should fall on a smooth trend between the two end-members. We
578 therefore calculated Fe^{2+}_{Td} site occupancies for different proportions of the total Fe^{2+} determined by XMCD
579 with the other Fe occupancies being controlled by stoichiometry. Continuous trends were found from 30 to
580 35% total Fe^{2+} in tetrahedral sites and we give data based on a proportion of $0.333 x Fe^{2+}_{total}$ in Td for the
581 three standard samples in Table 4 and show the full data set in Figure 8. This value of 0.333 matches that
582 for a fully disordered model for Fe. These data provide a plausible dataset for cation occupancies at high-T

583 in the spinel- magnetite solid solution series. The fact that the calculated M_s values for this new model are
584 only slightly higher than those for the XMCD model at 25°C confirms that the Mg tetrahedral occupancy
585 has more effect on the calculated value for M_s than the Fe oxidation ratio in the individual sites.
586 We commented earlier that the Fe L-edge spectra for the Fe-rich solid solutions indicate that the Fe
587 bonding characteristics over the composition range $Mgt_{1.0-0.51}$ are very similar and we speculated that these
588 solid solutions might show a degree of Fe clustering similar in structure to that in end-member magnetite.
589 This suggestion is supported by the XMCD measurements for these samples at 25°C showing an almost
590 linear trend for Fe^{3+}_{Td} while the Fe^{2+}_{Td} values are very small or zero, consistent with end-member magnetite
591 being a fully ordered, inverse spinel at room-T. We attempted to test this hypothesis further by using the Fe
592 K-edge EXAFS spectra to refine the proportions of Al (note that the X-ray scattering factors for Al and Mg
593 are essentially the same) *vs* Fe in the next nearest neighbour (NNN) cation shells. These define peaks at 3.0
594 Å (denoted FT3), where scatterers only occur in Oh, and at 3.5 Å (FT4, scatterers in both Oh and Td) in the
595 Fourier transform for spinels (Henderson et al., 2007). However, this failed as there were too many
596 variables to refine. We therefore refined four simple models for sample SP50: (i) Fe as the only NNN
597 scatterers in both FT3 and FT4 sites which gave an R factor of 68.2; (ii) Fe as the NNN scatterer in FT4 and
598 Al in FT3 (R = 68.6); (iii) Fe as the NNN scatterer in FT3 and Al in FT4 (R = 68.6); (iv) only Al in both
599 FT3 and FT4 (R = 95.0). As would be expected model (iv) is not probable. Model (i) shows the lowest R
600 factor but that value is not significantly different to that for models (ii) and (iii). Thus the EXAFS data
601 cannot be used to estimate the proportion of Al (+Mg) to Fe as NNN scatterers around the central target Fe.
602 Nevertheless, the Fe *L*-edge XAS and XMCD results, together with refined EXAFS model spectra for the
603 Fe-rich samples, are consistent with the presence of some Fe clustering to form nano-domains on a length
604 scale of a few unit cells (i.e., smaller than ~100 Å). Such nuclei would be too small (or would lack
605 periodicitiy) so that the Fe-rich solid solution samples have long-range 'homogeneous' structures on a
606 length scale probed by X-ray and neutron diffraction. Support for this suggestion is provided for another
607 sample of composition Mgt_{50} (SP11), for which Harrison and Putnis (1995) describe diffuse scattering at
608 the base of intense diffraction peaks. Thus it seems that solid solutions in the range ~$Mgt_{0.30}$ to ~ $Mg_{0.90}$ lie
609 inside a wide solvus (Mattioli and Wood, 1988; Harrison and Putnis, 1997a) at low-T and might contain
610 proto-nuclei of potential exsolved phases; this is indeed what the local structure indicates.

611 By contrast, Fe *L*-edge spectroscopy of Mg-rich solid solutions (SP3 and SP5) show very a
612 different electronic structure to that for the more Fe-rich samples reflecting a more homogeneous
613 arrangement of Fe, Mg and Al cations. In addition, replacement of Al for Fe^{3+} (electronegativities 1.5 and
614 1.71, respectively, Lenglet, 2004) and of Mg for Fe^{2+} (1.22 and 1.69) should produce more ionic structures
615 which could account for the better resolved *L*-edge features with a larger gap in energy between the Fe^{3+}
616 and Fe^{2+} spectral features. Sample SP9 ($Mgt_{0.41}$) seems to have mixed bonding characteristics (see earlier)
617 and must lie well inside the solvus but we expect that samples SP5 ($Mgt_{0.23}$) and SP3 ($Mgt_{0.17}$) definitely lie
618 within the single-phase field. The *L*-edge spectrum for the natural magnesian spinel studied by Cressey et
619 al. (1993), with the composition $Mgt_{0.20}$ also exhibits a large energy gap between the Fe^{3+} and Fe^{2+} spectral
620 features and should also be truly single phase. Support for this suggestion comes from a high-resolution
621 XRD study (P.F. Schofield, pers. comm., 2015) which shows very sharp diffraction peaks, without
622 broadened flanks suggesting diffuse scattering, and without any peaks due to an exsolved, more Fe-rich
623 spinel phase. The natural sample will have cooled very slowly, unlike our synthetic samples, with ample
624 opportunity for exsolution to occur if its composition lay within the spinel-magnetite solvus.
625 Harrison et al. (1999) discussed the significance of relating site occupancies deduced for the solid
626 solutions at high-T to magnetic properties measured at low-T but we have shown that the distribution of Fe
627 between the two sites has more effect on the size of M_s than the variation of Fe oxidation ratio between
628 individual sites. The high-T site occupancies determined by Harrison et al. (1999) clearly match the
629 measured magnetic properties (Harrison and Putnis, 1995, 1996, 1997b) better than those of Nell and Wood
630 (1989) as shown in Table 4. The XMCD site occupancies should be directly comparable to the low-T
631 magnetic measurements as both were carried out on quenched samples which are likely to have undergone
632 electron exchange reactions over both sites. In Figure 9, we compare our calculated saturation
633 magnetisation data with the values measured by Harrison and Putnis (1995). It is clear that the trends are
634 very similar with the data for more Fe-rich samples overlapping, while our M_s values for more magnesian
635 solid solutions show a well-defined flat trend up to $Mgt_{0.5}$ but this trend is displaced to higher values than
636 those for the macroscopic measured magnetic data. Our calculated M_s for the Mg-rich solid solutions were
637 obtained assuming that the magnetic moments on the octahedral and tetrahedral sites were exactly anti-
638 parallel as is the case for magnetite-rich samples (Néel, 1955). However, Harrison and Putnis (1999)

639 concluded that measured low saturation magnetisation values for the Mg and Al-rich solid solutions could
640 reflect departure from a co-linear ferrimagnetic spin structure due to the high dilution of the magnetic
641 cations and it is likely that our calculated M_s are too high for that reason. The overall agreement between
642 the magnetic properties calculated from our site occupancy data and the measured values is further evidence
643 in support of our conclusion that the surface compositions of our samples match those of the bulk.
644

645 **IMPLICATIONS**

646 Fe $L_{2,3}$ XAS and XMCD spectroscopies and Mg and Fe K-edge XANES and EXAFS measured at
647 room-T for samples in the solid solution series $MgAl_2O_4$ – Fe_3O_4 (Mgt) show that Fe bonding features vary
648 depending on bulk composition. The presence of a solvus in the system over the composition range $Mgt_{0.3}$
649 to $Mgt_{0.9}$ means that local pair-wise repulsive interactions (e.g., Fe^{3+} - Al, or Fe^{2+} - Mg interactions) drive
650 the system to cluster into spinel-rich and magnetite-rich regions on a tens-of-Å length-scale which is too
651 small to be detected by X-ray and neutron diffraction techniques. The lack of Fe^{2+}_{Td} at the magnetite-rich
652 end is caused by quench re-ordering via rapid electron hopping. Some quenching of tetrahedral Fe^{2+} is
653 observed in the centre of the solid solution, as electron hopping between Td and Oh sites is less favourable
654 when Mg and Al are present in significant amounts. The most Mg-rich samples studied ($Mgt_{0.17}$ and $Mgt_{0.23}$)
655 have short range Fe bonding features different to those typical of magnetite and we conclude that Fe-atoms
656 are not clustered because of dilution of Fe by Mg and Al over both the octahedral and tetrahedral sites. The
657 apparent lack of Fe^{2+}_{Td} at the spinel-rich end mainly reflects XMCD fitting problems due to weak magnetic
658 scattering of low-Fe samples which were studied at room-T, i.e., above their Curie temperatures. In
659 addition, the increased energy separation between Fe^{2+} and Fe^{3+} spectral features results in overlap of
660 XMCD spectral features for Fe cations with the same oxidation state but in different crystallographic sites.

661 Magnetic properties are consistent with this model, accounting for: i) low M_s values and low *Tc*
662 values at the spinel-rich end, and ii) better agreement between calculated and observed M_s at the magnetite-
663 rich end.

664 Analytical and spectroscopic evidence for synthetic and natural Mg-rich spinels (~$Mgt_{0.15\text{-}0.25}$) are
665 consistent with the Fe-rich component being more reduced than the assumed stoichiometry (i.e., (Fe^{3+}/Total

Fe ~0.5 rather than 0.66) suggesting the possibility of a changed equilibrium stoichiometry at the spinel-rich end of the spinel-magnetite solid solution series.

The study of samples across this whole solid solution series provides much value-added structural information, over and above that obtained for end-members, and could be applied to other binary spinel solid solutions.

ACKNOWLEDGEMENTS.

We thank Richard Pattrick and Vicky Coker for help in collecting XMCD on these samples at the Daresbury SRS and subsequently at the Advanced Light Source (ALS), Berkeley. The ALS is supported by the Director, Office of Science, Office of Basic Energy Sciences (OBES) of the U.S. Department of Energy (DOE) under Contract No. DE-AC02-05CH11231 and we thank Elke Arenholz for her assistance. RJH acknowledges funding from the European Research Council under the European Union's Seventh Framework Programme (FP/2007-2013)/ERC Grant Agreement No. 320750. KMR gratefully acknowledges support from the DOE OBES Chemical Sciences, Geosciences, and Biosciences Division, through the Geosciences Program at Pacific Northwest National Laboratory. We also thank Gerrit van der Laan and Nick Telling for help with XMCD data analysis; David Plant carried out the electron microprobe analyses at Manchester and Paul Schofield provided information on the natural magnesian spinel. We also thank two anonymous referees for constructive comments.

685 **REFERENCES**

686 Andreozzi, G.B., and Lucchesi, S.G. (2002) Intersite distribution of Fe^{2+} and Mg in spinel (sensu strico) –
687 hercynite series by single-crystal X-ray diffraction. American Mineralogist, 87, 1113-1120.
688 Arenholz, E., and Prestemon, S.O. (2005) Design and performance of an eight-pole resistive magnet for soft
689 X-ray magnetic dichroism measurements. Review Scientific Instruments, 76, 083908/1-8.
690 Bahgat, A.A., Fayek, M.K., Hamalaway, A.A., and Eissa, N.A. (1980) The influence of substitution of iron
691 ions on the electron hopping in magnetite. Journal of Physics C: Solid State Physics, 13, 2601-
692 2608.
693 Becker, K.D. (2001) In situ spectroscopy in solid state chemistry. Solid State Ionics, 141-142, 21-30.
694 Berry, A.J., O'Neill, H.St C., Javasuriya, K.D., Campbell, S.J., and Foran, G.J. (2003) XANES
695 calibrations for the oxidation state of iron in a silicate glass. American Mineralogist, 88, 967-977.
696 Binsted, N. (1998) Daresbury Laboratory EXCURV98 Program.
697 Brown, G.E. Jr, Calas, G., Waychunas, G.A., and Petiau, J. (1995) X-ray absorption spectroscopy and its
698 applications in mineralogy and geochemistry. Reviews in Mineralogy (American Mineralogical
699 Society), 18, 431-512.
700 Byrne, J.M., Coker, V.S., Moise, S., Wincott, P.L., Vaughan, D.J., Tuna, F., Arenholz, E., van der Laan, G.,
701 Pattrick, R.A.D., Lloyd ,J.R., and Telling, N.D. (2013) Controlled cobalt doping in biogenic
702 magnetite nanoparticles Journal Royal Society Interface, 10, 2013.0134.
703 Carbonin, S., Russo, U., and Della Giusta, A. (1996) Cation distribution in some natural spinels from X-
704 ray diffraction and Mössbauer spectroscopy. Mineralogical Magazine, 60, 355-368.
705 Cressey, G., Henderson, C.M.B., and van der Laan, G. (1993) Use of L-edge X-ray absorption
706 spectroscopy to characterize multiple valence states of 3d transition metals; a new probe for
707 mineralogical and geochemical research. Physics and Chemistry of Minerals, 20, 111-119.
708 Della Giusta, A., Carbonin, S., and Ottonello, G. (1996) Temperature-dependent disorder in a natural Mg-
709 Al-Fe^{2+}-Fe^{3+} - spinel. Mineralogical Magazine, 60, 603-616.
710 Dieckmann, R., and Schmalzreid, H. (1977a) Defects and cation diffusion in magnetite (I). Berichte der
711 Bunsen Gesellschaft, 81, 344-347.

712 Dieckmann, R., and Schmalzreid, H. (1977b) Defects and cation diffusion in magnetite (II). Berichte der
713 Bunsen Gesellschaft, 81, 414-419.
714 Dieckmann, R., Witt, C.A., and Mason, T. (1983) Defects and cation diffusion in magnetite (V): electrical
715 conduction, cation distribution and point defects in $Fe_{3-\delta}O_4$. Berichte der Bunsengesselschaft für
716 physikalische Chemie, 87, 495-503.
717 Doriguetto, A.C., Fernandes, N.G., Persiano, A.I.C., Filho, E.N., Grenèche, J.M., and Fabris, J.D. (2003)
718 Characterization of a natural magnetite. Physics and Chemistry of Minerals, 30, 249-255.
719 Droop, G.T.R. (1987) A general equation for estimating Fe^{3+} concentrations in ferro-magnesian silicates
720 and oxides from microprobe analyses, using stoichiometric criteria. Mineralogical Magazine, 51,
721 431-435.
722 Eisenberger, P., and Brown, G.S. (1979) The study of disordered systems by EXAFS: limitations. Solid
723 State Communications, 29, 481-484.
724 Fleet, M.E. (1981) The structure of magnetite. Acta Crystallographica B, 37, 917-920.
725 Fleet, M.E. (1982) The structure of magnetite; defect structure II. Acta Crystallographica B**,** 38, 1718-
726 1723.
727 Gilbert, B,, Katz, J.E., Denlinger, J.D., Yin,Y., Falcone, R., and Waychunas, G.A. (2010) Soft X-ray
728 spectroscopy study of the electronic structure of oxidized and partially oxidised magnetite
729 nanoparticles. Journal of Physical Chemistry, 114, 21994-22001.
730 Goering, E., Gold, S., Lafkioti, M., and Sch□tz, G. (2006) Vanishing Fe 3d orbital moments in single-
731 crystalline magnetite. Europhysics Letters, 73, 97-103.
732 Goodenough, J.B., and Loeb, A.L. (1955) Theory of ionic ordering, crystal distortion, and magnetic
733 exchange due to covalent forces in spinels. Physical Review, 98, 391-408.
734 Gota, S., Gautier-Soyer, M., and Sacchi, M. (2000) Fe 2*p* absorption in magnetic oxides: Quantifying
735 angular-dependent saturation effects. Physical Review B, 62, 4187-4190.
736 Graf, C., Goroncy, C., Stumpf, P., Weschke, E., Boeglin, C., Ronneburg, H., and R□hl, E. (2015) Local
737 magnetic and electronic structure of the surface region of postsynthetic oxidized iron oxide
738 nanoparticles for magnetic resonance imaging. Journal of Physical Chemistry, 119, 19404-19414.

739 Gunjakar, J.L., More, A.M., Gurav,C.D., and Lokhande, C.D. (2008) Chemical synthesis of spinel nickel
740 ferrite ($NiFe_2O_4$) nano-sheets. Applied Surface Science**,** 254, 5844-5848.
741 Gurman, S.J., Binsted, N., and Ross, I. (1984) A rapid, exact, curved-wave theory for EXAFS calculations.
742 Journal Physics C, 17, 143-151.
743 Harrison, R.J. (1997) Magnetic properties of the magnetite-spinel solid solution: Curie temperatures,
744 magnetic susceptibilities and cation ordering. Ph.D. Thesis, University of Cambridge, UK.
745 Harrison, R.J., and Putnis, A. (1995) Magnetic properties of the magnetite-spinel solid solution: Saturation
746 magnetization and cation distributions. American Mineralogist, 80, 213-221.
747 Harrison, R.J., and Putnis, A. (1996) Magnetic properties of the magnetite-spinel solid solution: Curie
748 temperatures, magnetic susceptibilities, and cation ordering. American Mineralogist, 81, 375-384.
749 Harrison R.J., and Putnis A. (1997a) Interaction between exsolution microstructures and magnetic
750 properties of the magnetite-spinel solid solution. American Mineralogist, 82, 131-142.
751 Harrison, R.J., and Putnis, A. (1997b) The coupling between magnetic and cation ordering: a macroscopic
752 approach. European Journal of Mineralogy, 9, 1115-1130.
753 Harrison, R.J., and Putnis, A.W. (1999) The magnetic properties and crystal chemistry of oxide spinel solid
754 solutions. Surveys in Geophysics**,** 19, 461-520.
755 Harrison, R.J., Dove, M.T., Knight, K.S., and Putnis, A. (1999) In-situ diffraction study of non-convergent
756 cation ordering in the $(Fe_3O_4)_{1-x}(MgAl_2O_4)_x$ spinel solid solution. American Mineralogist, 84, 555-
757 563.
758 Harrison, R.J., Redfern, S.A.T., and O'Neill, H. St C. (1998) The temperature dependence of the cation
759 distribution in synthetic hercynite ($FeAl_2O_4$) from in-situ neutron refinements. American
760 Mineralogist , 83, 1092-1099.
761 Henderson, C.M.B., Knight, K.S., Redfern, S.A.T., and Wood, B.J. (1996) High-temperature studies of
762 octahedral cation exchange in olivine by neutron powder diffraction. Science, 271, 1713-1715.
763 Henderson, C.M.B., Charnock, J.M., and Plant, D.A. (2007) Cation occupancies in Mg, Co, Ni, Zn, Al
764 ferrite spinels: A multi-element study. Journal of Physics: Condensed Matter, 19, 1-25.
765 Hill, R.J., Craig, J.R., and Gibbs, G.V. (1979) Systematics of the spinel structure type. Physics and
766 Chemistry of Minerals, 4, 317-349.

767 Holland, T.J.B., and Redfern, S.A.T. (1997) Unit-cell refinement from powder diffraction data: the use of
768 regression diagnostics. Mineralogical Magazine, **6**1, 65-77.
769 Huberty, J.M., Konishi, H., Heck, P.R., Fournelle, J.H., Valley, J.W., and Xu, H. (2012) Silician magnetite
770 from the Dales Gorge Member of the Brockamn Iron Formation, Hamersley Group, Western
771 Australia. American Mineralogist, 97, 26-37.
772 Ildefonse, Ph., Coala, G., Flank, A.M., and Lagarde, P. (1995) Low Z elements (Mg, Al, and Si) K-edge
773 absorption spectroscopy in minerals and disordered systems. Nuclear Instruments Methods Physics,
774 B97, 172-175.
775 Kuiper, P., Searle, B.G., Duda, L.-C., Wolf, R.M., and van der Zaag, P.J. (1997) Fe $L_{2,3}$ linear and circular
776 dochroism of Fe_3O_4. Journal of Electron Spectroscopy and Related Phenomena. 86, 107-113.
777 Lavina, B., Salviulo, G., and Della Giusta, A. (2002) Cation distribution and structure modelling of spinel
778 solid solutions. Physics and Chemistry of Minerals, 29, 10-18.
779 Lenglet, M. (2004) Iono-covalent character of the metal – oxygen bonds in oxides: a comparison of
780 experimental and theoretical data. Active and Passive Electronic Components, 27, 1-60.
781 Li, D., Peng, M., and Murata, T. (1999) Coordination and local structure of magnesium in silicate minerals
782 and glasses: Mg K-edge XANES study. The Canadian Mineralogist**,** 37, 199-206.
783 Lilova, K.I., Xu, F., Rosso, K.M., Pearce, C.I., Kamali, S., and Navrotsky, A. (2012) Oxide solution
784 calorimetry of Fe^{3+}-bearing oxides and application to the magnetite-maghemite (Fe_3O_4-$Fe_{8/3}O_4$)
785 system. American Mineralogist, 97, 164-175.
786 Lindsley, D.H. (1976) The crystal chemistry and structure of oxide minerals as exemplified by the Fe-Ti
787 oxides. Oxide Minerals, Mineralogical Society of America Short Course Notes**,** 3, L1-60.
788 Liu, C., Zou, B., Rondinone, A.J., and Zhang, J. (2000) Chemical control of superparamagnetic properties
789 of magnesium and cobalt spinel ferrite nanoparticles through atomic level magnetic couplings.
790 Journal American Chemical Society, 122, 6263-6267.
791 Marco, J.F., Gancedo, R., Gracia, M., Gautier, J.L., Rios, E.I., Palmer, H.M., Greaves, C., and Berry, F.J.
792 (2001) Cation distribution and magnetic structure of the ferrimagnetic spinel $NiCo_2O_4$. Journal of
793 Materials Chemistry, 11, 3087-3093.

794 Marshall, C.P., and Dollase, W.A. (1984) Cation arrangement in iron-zinc-chromium spinel oxides.
795 American Mineralogist, 69, 928-936.
796 Martignano, F., Andreozzi, G.B., and Dal Negro, A. (2006) Thermodynamics and kinetics of cation
797 ordering in natural and synthetic $Mg(Al,Fe^{3+})_2O_4$ spinels from in situ high-temperature X-ray
798 diffraction. American Mineralogist, 91**,** 306-312.
799 Mattioli, G.S., and Wood, B.J. (1988) Magnetite activities across the $MgAl_2O_4$ – Fe_3O_4 spinel join with
800 application to the thermobarometric estimates of upper mantle oxygen fugacity. Contributions to
801 Mineralogy and Petrology, 98, 148-162.
802 Nakajima, R., Stöhr, J., and Idzerda, Y.U. (1999) Electron-yield saturation effects in *L*-edge x-ray
803 magnetic circular dichroism spectra of Fe, Co and Ni. Physical Review B, 59, 6421-6429.
804 Nakatsuka, A., Ueno, H., Nakayama, N., Mizota,T., and Maekawa, H. (2004) Single-crystal X-ray
805 diffraction study of cation distribution in $MgAl_2O_4$-$MgFe_2O_4$ spinel solid solution Physics and
806 Chemistry of Minerals, 31, 278-287.
807 Navrotsky, A., and Kleppa, O.J. (1968) Thermodynamics of formation of simple spinels. Journal of
808 Inorganic and Nuclear Chemistry, 30, 479-498.
809 Néel, L. (1955) Some aspects of rock magnetism. Advances in Physics**,** 4, 191-243.
810 Nell, J., Wood, B.J., and Mason, T.O. (1989) Thermodynamic properties in a multicomponent solid
811 solution involving cation disorder: Fe_3O_4 - $MgAl_2O_4$ - $MgFe_2O_4$ - $FeAl_2O_4$. American Mineralogist**,**
812 74**,** 1000-1015.
813 Nell, J., and Wood, B.J. (1989) High-temperature cation distributions in Fe_3O_4-$MgAl_2O_4$-$MgFe_2O_4$-$FeAl_2O_4$
814 spinels from thermopower and conductivity measurements. American Mineralogist, 74. 339-351.
815 O'Neill, H.StC., and Navrotsky, A. (1983) Simple spinels: crystallographic parameters, cation radii, lattice
816 energies, and cation distribution. American Mineralogist, 68, 181-194.
817 O'Neill, H.StC., and Navrotsky, A. (1984) Cation distributions and thermodynamic properties of binary
818 spinel solid solutions. American Mineralogist, 69, 733-753.
819 O'Neill, H.StC., Annersten, H., and Virgo, D. (1992) The temperature dependence of the cation distribution
820 in magnesioferrite ($MgFe_2O_4$) from powder XRD structural refinements and Mőssbauer
821 spectroscopy. American Mineralogist **,** 77, 725-740.

822 Palin, E.J., and Harrison, R.J. (2007) A computational investigation of cation ordering phenomena in the
823 binary spinel system $MgAl_2O_4$ – $FeAl_2O_4$. Mineralogical Magazine, 71, 611-624.
824 Parker, R., and Tinsley, C.J. (1976) Electrical conduction in magnetite. Physica Status Solidi, A, 88, 189-
825 194.
826 Pattrick, R.A.D., van der Laan, G., Henderson, C.M.B., Kuiper, P., Dudzik, E., and Vaughan, D.J. (2002)
827 Cation site occupancy in spinel ferrites studied by X-ray magnetic circular dichroism: developing a
828 method for mineralogists. European Journal of Mineralogy, 14, 1095-1102.
829 Pearce, C.I., Henderson, C.M.B., Pattrick, R,.A.D., van der Laan, G., and Vaughan, D.J. (2006) Direct
830 determination of cation site occupancies in natural ferrite spinels by $L_{2,3}$ X-ray absorption
831 spectroscopy and X-ray magnetic circular dichroism. American Mineralogist, 91, 880-893.
832 Pearce, C.I., Henderson, C.M.B., Telling, N.D., Pattrick, R.A.D., Charnock, J.M., Coker, V.S., Arenholz,
833 E., Tuna, F., and van der Laan, G. (2010) Fe site occupancy in magnetite – ulvöspinel solid
834 solutions: a new approach using X-ray magnetic circular dichroism. American Mineralogist, 95,
835 425-430.
836 Pearce, C.I., Qafoku, O., Liu, J., Arenholz, E., Heald, S.M., Kukkadapu, R. K., Gorski, C..A., Henderson,
837 C.M.B., and Rosso, K.M. (2012) Synthesis and properties of titanomagnetite ($Fe_{3-x}Ti_xO_4$)
838 nanoparticles: A tunable solid-state Fe(II/III) redox system. Journal of Colloid Interface Science,
839 387, 24-38.
840 Pellegrin, E., Hagelstein, M., Doyle, S., Moser, H.O., Fuchs, J., Vollath, D., Schuppler, S., James, M.A.,
841 Saxena, S.S., Nielsen, L., Rogajanu, O., Sawatzky, G.A., Ferrero, C., Borowski, M., Tjernberg, O.,
842 and Brookes, N. (1999) Characterization of nanocrystalline γ-Fe_3O_4 with synchrotron radiation
843 techniques. Physica Status Solidi B, 215, 797-801.
844 Peng, G., van Elp, J., Que, L. Jr, Armstrong, W.H., and Cramer, S.P. (1995) L-edge X-ray absorption and
845 X-ray magnetic circular dichroism of oxygen-bridged dinuclear iron complexes. Journal American
846 Chemical Society, 117, 2515-2519.
847 Redfern, S.A.T., Harrison, R.J., O'Neill, H. St C., and Wood, D.R.R. (1999) Thermodynamics and kinetics
848 of cation ordering in $MgAl_2O_4$ spinel up to 1600°C from in situ neutron diffraction. American
849 Mineralogist, 84, 299-310.

850 Schedin, F., Hill, E.W., van der Laan, G., and Thornton, G. (2004) magnetic properties of stoichiometric
851 and nonstoichiometric ultrathin Fe_3O_4(111) films on Al_2O_3(0001). Journal of Applied Physics, 96,
852 1165-1169.
853 Shannon, R.D. (1976) Revised effective ionic radii and systematic studies of interatomic distances in
854 halides and chalcogenides Acta Crystallographica A**,** 32, 751-767.
855 Tiano, A.L., Papaefthymiou, G.C., Lewis, C.S., Han, J., Zhang, C., Li, Q., Shi, C., Abeykoon, A.M.M.,
856 Billinge, S.J.L., Stach, E., Thomas, J., Guerro, K., Munayco, J., Scorzelli, R.B., Burnham, P.,
857 Viescas, A.J., and Wong, S.S. 2015 Correlating size and composition-dependent effects with
858 magnetic, Mössbauer, and pair distribution function measurements in a family of catalytically
859 active ferrite nanoparticles. Chemistry of Materials, 27, 3572-3592.
860 Uchida, H., Lavina, B., Downs, R.T., and Chesley, J. (2005) Single-crystal X-ray diffraction of spinels
861 from the San Carlos Volcanic Field, Arizona: spinel as a geothermometer. American Mineralogist,
862 90, 1900-1908.
863 Trcera, N., Cabaret, D., Rossano, S., Farges, F., Flank, An.-M., and Lagarde, P. (2009) Mg K-edge
864 XANES spectra in crystals and oxide glasses: Experimental vs. theoretical approaches. Physics and
865 Chemistry of Minerals, 36**,** 241-257.
866 van der Laan, G., and Kirkman, I. W. (1992) The 2p absorption spectra of 3d transition metal compounds in
867 tetrahedral and octahedral symmetry. Journal of Physics: Condensed Matter, 4, 4189–4204.
868 van der Laan, G., and Thole, B. T. (1991) Strong magnetic X-ray dichroism in 2p absorption spectra of 3d
869 transition metal ions. Physical Review B, 43, 13401–13411.
870 van der Laan, G., and Figueroa, A.L. (2014) X-ray magnetic circular dichroism – A valuable tool to study
871 magnetism. Coordination Chemistry Reviews, 277-278, 95-129.
872 Verwey, E.J., Haayman, P.W., and Romeijn, F.C. (1947) Physical properties and cation arrangement of
873 oxides with spinel structures. II. Electronic conductivity. Journal of Chemical Physics, 15, 181-
874 187.
875 Waerenborgh, J.C., Figueiredo, M.O., Cabral, J.M.P., and Pereira, L.C.J. (1994) Powder XRD structure
876 refinements and ^{57}Fe Mössbauer effect study of synthetic $Zn_{1-x}Fe_xAl_2O_4$ ($0 < x \leq 1$) spinels
877 annealed at different temperatures. Physics and Chemistry of Minerals, 21, 460-468.

878 Waychunas G A (1991) Crystal chemistry of oxides and oxyhydroxides. Reviews in Mineralogy
879 (Mineralogical Society of America), 25, 11-68.
880 Wißmann, S., Wurmb, V.v., Litterst, F.J., Dieckmann, R., and Becker, K.D. (1998) The temperature
881 dependent cation distribution in magnetite. Journal Physics and Chemistry of Solids, 59, 321-330.
882 Wu, C.C., and Mason, T.O. (1981) Thermopower measurement of cation distribution in magnetite. Journal
883 of the American Ceramic Society, 64, 520-522.
884 Yamanaka, T., and Takéuchi, Y. (1983) Order – disorder transition in $MgAl_2O_4$ spinel at high temperatures
885 up to 1700°C. Zeitshrift f□r Krisallographie, 165**,** 65-78.
886 Zhu, X., Kilirai, S.S., Hitchcock, A.P., and Bazylinski, D.A. (2015) What is the correct Fe $L_{2,3}$ X-ray
887 absorption spectrum of magnetite? Journal of Electron Spectroscopy and Related Phenomena, 199,
888 19-26.
889

Figure captions.

Figure 1. Mg K-edge XANES spectra of spinels from the solid solution series $MgAl_2O_4 – Fe_3O_4$. From bottom up: Sample SP14, $(Fe_3O_4)_{0.81}(MgAl_2O_4)_{0.19}$ (denoted $Mgt_{0.81}$); SP13, $Mgt_{0.61}$; SP50, $Mgt_{0.51}$; SP9, $Mgt_{0.41}$; SP5, $Mgt_{0.23}$; $MgAl_2O_4$, $Mgt_{0.0}$. The progressive decrease in size of the first peak at 1309 eV with increasing Mgt content can be correlated with the decreasing proportion of total Mg occurring in the tetrahedral site.

Figure 2. Fe K-edge XANES of spinels from the solid solution series $MgAl_2O_4 – Fe_3O_4$. From bottom up: Fe_3O_4, $Mgt_{1.00}$: SP14, $Mgt_{0.81}$; SP13, $Mgt_{0.61}$; SP50, $Mgt_{0.51}$; SP9, $Mgt_{0.41}$; SP5, $Mgt_{0.23}$. See text for further explanation.

Figure 3. Fe $L_{2,3}$ XAS spectra (black lines) of spinels from the solid solution series $MgAl_2O_4 – Fe_3O_4$. Compositions as follows: SP3, $Mgt_{0.17}$; SP5, $Mgt_{0.23}$; SP9, $Mgt_{0.41}$; SP50, $Mgt_{0.51}$; SP20, $Mgt_{0.55}$; SP13, $Mgt_{0.61}$; SP17, $Mgt_{0.71}$; SP14, $Mgt_{0.81}$. The XAS peak intensities are scaled to the same height for all samples so that small changes in peak shape are clear. The red lines show the XMCD difference spectra and reflect the compositional differences with the XMCD peak intensity increasing with increasing bulk Fe content.

Figure 4. $L_{2,3}$ XMCD experimental spectra (open symbols in left-hand panel) and summed fits (red lines in left-hand panel) for spinels from the solid solution series $MgAl_2O_4 – Fe_3O_4$. Compositions as follows: SP3, $Mgt_{0.17}$; SP5, $Mgt_{0.23}$; SP9, $Mgt_{0.41}$; SP50, $Mgt_{0.51}$; SP20, $Mgt_{0.55}$; SP13, $Mgt_{0.61}$; SP17, $Mgt_{0.71}$; SP14, $Mgt_{0.81}$. The right hand panel shows spectral fits for the four Fe-components; colours as labelled in panel for SP9: red Fe^{2+}_{Td}; black Fe^{2+}_{Oh}; blue Fe^{3+}_{Td}; green Fe^{3+}_{Oh}. The y axis for each panel is calibrated and shows the relative strengths of the XMCD signals for each sample (see correct relative XMCD peak intensities in Figure 3).

Figure 5. Relationship between XMCD peak heights and bulk composition for ferrimagnetic samples (small solid diamonds) and paramagnetic samples (larger solid squares). Symbol sizes are in proportion to likely XMCD errors. All data were determined at room temperature except for sample SP9 ($Mgt_{0.39}$) where data were obtained at 20K which is below its Curie temperature (T_c). Linear fits for ferrimagnetic samples (i.e., XMCD data obtained below T_c) show much larger signals than those for paramagnetic samples (data above T_c). Note that the XMCD intensity for ferrimagnetic SP9 at $Mgt_{0.39}$ is over 2x that for the paramagnetic species (temperatures 20K and 298K respectively).

Figure 6. Cation site occupancies calculated to 4 oxygens pfu as a function of solid solution composition based on XMCD spectra obtained at room temperature (298K). Fig. 6a shows the measured XMCD values

926 for Fe^{2+} and Fe^{3+} in the tetrahedral site, together with 10% total Al allocated to Td, with Mg added to bring
927 the site occupancy to 1.000. Fig. 6b shows the measured Fe^{2+} and Fe^{3+} octahedral site occupancies together
928 with the remaining Al (90% of total Al) and Mg. See text for detailed explanation and discussion.
929
930 Figure 7. Compositional dependence of cation site occupancies based on the high-T disordered, pseudo-
931 random model of Harrison et al. (1999). In this model 10% of total Al was allocated to the tetrahedral site;
932 XMCD measured total Fe^{2+} and total Fe^{3+}, together with Mg, were then allocated to fill the Td site (1.000
933 atoms pfu) in strict proportion to their total contents. The octahedral site contains all the remaining Fe^{2+},
934 Fe^{3+}, Mg and Al. The data shown for end-member magnetite assume a fully disordered structure. See text
935 for further explanation.
936
937 Figure 8. Hypothetical high-T model showing the compositional dependence of cation site occupancies. In
938 this model the Mg and Al occupancies for Td and Oh sites are the same as those shown in Table 3 and
939 Figure 6. The XMCD data are used to fix the total Fe^{2+} and Fe^{3+} concentrations and then Fe is allocated to
940 fill the tetrahedral site proportion using different proportions of total Fe^{2+}:Fe^{3+}. The remaining Fe^{2+} and Fe^{3+}
941 are then added to the octahedral site. This process was repeated until the trends shown for the different Fe-
942 occupancies merged with the fully disordered data points for end-member magnetite (e.g., Fe^{2+}_{Td} at 0.333
943 apfu). See text for further explanation and discussion.
944
945 Figure 9. Variation of saturation magnetic moment (M_s) with composition for magnetic spinels in the
946 system $MgAl_2O_4 – Fe_3O_4$. Solid squares are values measured on quenched synthetic samples (Harrison and
947 Putnis, 1995). Open triangles are M_s values calculated from cation occupancies based on XMCD Fe
948 measurements at room-T (see Table 3) assuming that electron spins are exactly anti-parallel on octahedral
949 and tetrahedral sites (Néel, 1955). Solid triangles are calculated from site occupancies for the hypothetical
950 high-T model shown in Figure 8 (this paper). The higher M_s values for the high-T model reflect the higher
951 Fe^{2+}_{Td} and lower Fe^{3+}_{Td} values compared to room-T XMCD model data.
952

Table 1. Analyses and cell formulae for synthetic $MgAl_2O_4$ – Fe_3O_4 solid solutions and XMCD data for Fe^{2+} and Fe^{3+} proportions at room T (298 K)
and for SP9 at 20 K (i.e., below its Curie temperature).

	SP3	SP5	SP9		SP50	SP20	SP13	SP1
	Harrison & Putnis (1995)	Harrison & Putnis (1995)	This paper Average of 10		This paper Average of 12	This paper Average of 18	Harrison & Putnis (1995)	Harı
Fe_3O_4 (molecular %)	16.5(2)[%]	23.4(2)	40.5(5)		50.6(5)	55.4(6)	60.8(9)	71.0
Wt.%								
SiO_2	0.26[$](8)[%]	0.22[$](9)	0.02[$](1)		0.09(8)	0.01(1)	0.06[$](2)	0.02
Al_2O_3	55.4(6)	48.5(2)	34.1(5)		27.2(4)	23.9(7)	20.5(1.5)	14.3
Total Fe as FeO	23.0(2)	31.1(1)	49.4(5)		58.6(7)	62.4(8)	67.5(1.5)	74.3
Fe_2O_3[*]	15.6	22.3	36.7		43.0	45.9	50.0	55.0
FeO[*]	8.9	11.0	16.4		19.9	21.1	22.6	24.8
MgO	21.2(2)	18.9(1)	13.6(1)		10.6(3)	9.2(2)	8.1(3)	5.7
Total	101.4	100.9	100.8		100.8	100.1	101.2	99.8
Cats/4(O), 3cats								
Si	0.007(2)	0.006(2)	0.0005(2)		0.003(2)	0.0003(2)	0.002(1)	0.00
Al	1.68(2)[&]	1.537(6)	1.18(2)		0.993(14)	0.90(3)	0.78(6)	0.57
Fe^{3+}	0.303	0.451	0.814		1.002	1.100	1.216	1.42
Fe^{2+}	0.192	0.248	0.403		0.515	0.562	0.612	0.71
Mg	0.817(8)	0.758(4)	0.597(4)		0.487(13)	0.438(9)	0.390(14)	0.29
Total Fe atoms[&]	0.494(4)	0.699(15)	1.217(12)		1.517(18)	1.662(21)	1.83(4)	2.13
Atom $Fe^{3+}/(Fe^{3+}+Fe^{2+})$	0.612	0.645	0.669		0.661	0.662	0.665	0.66
Curie temp.(K)[+]	~20	~20	215		380	440	505	615
Cell edge, Å[^]	8.141(1)	8.169(1)	8.233(2)		8.262(2)	8.268(2)	8.293(2)	8.32
Cats/4(O) for XMCD Fe^{2+} and Fe^{3+} props.			298 K	20K				
Si	0.007(2)	0.006(2)	0.0005(2)	0.0005(2)	0.003(2)	0.0003(2)	0.002(1)	0.00
Al	1.69(2)	1.553(6)	1.18(2)	1.18(2)	0.994(14)	0.90(3)	0.79(6)	0.59
[#]Fe^{3+}	0.25(4)	0.37(4)	0.85(3)	0.78(2)	0.98(2)	1.06(2)	1.09(2)	1.27
[#]Fe^{2+}	0.24(4)	0.33(4)	0.37(3)	0.44(2)	0.54(2)	0.61(2)	0.77(2)	0.91
Mg	0.822(8)	0.763(15)	0.600(4)	0.600(4)	0.490(13)	0.442(9)	0.396(14)	0.29
Cation total	3.017	3.023	3.000	3.000	3.008	3.015	3.049	3.06
Total Fe atoms	0.495(4)	0.701(15)	1.218(12)	1.219(12)	1.521(18)	1.670(21)	1.86(4)	2.17
XMCD: Atom $Fe^{3+}/(Fe^{3+}+Fe^{2+})$	0.512	0.536	0.694	0.637	0.647	0.637	0.587	0.58

[$] SiO_2 concentrations determined for this paper; [%]Numbers in brackets are estimated 1 sigma errors for last place(s); [*] Calculated for 3 cations and 4 oxygens pfu;
[+] From Harrison and Putnis (1996); [^] From Harrison and Putnis (1995; 1997); [&] Errors assumed to be the same as for wt.% analytical values; [#] Errors for XMCD determined Fe^{2+} and Fe^{3+} are 1-2% relative for Fe-rich ferrimagnetic samples and 5-10% for Fe-poor paramagnetic samples.

966 Table 2. K-edge EXAFS parameters for Fe and Mg in spinel - magnetite ($MgAl_2O_4 – Fe_3O_4$) solid
967 solutions and fitted M – O bond lengths and cation occupancies for the
968 tetrahedral and octahedral sites.
969

Sample	Element	K-edge energy, eV	Pre-edge/ Edge at ½ height	Tetrahedral Site Td			Octahedral Site, Oh		
				R, Å	Proportion in Td , %	Normalised occupancy	R, Å	Proportion in Oh, %	Normalised occupancy
SP5, $Mgt_{0.23}$	Fe Mg *Estimated Al*	7117.0	0.06	1.84 1.97	45 54	0.32 0.41 *0.27 (18%)*	1.97 2.12	55 46	0.38 0.35 *1.27*
SP9, $Mgt_{0.41}$	Fe Mg *Estimated Al*	7117.0	0.06	1.84 2.00	45 47	0.52 0.28 *0.20 (16%)*	1.96 2.10	55 53	0.64 0.32 *1.04*
SP50, $Mgt_{0.51}$	Fe Mg *Estimated Al*	7117.3	0.06	1.83 2.00	40 45	0.61 0.23 *0.15 (15%)*	1.97 2.06	60 55	0.91 0.28 *0.81*
SP13, $Mgt_{0.61}$	Fe Mg *Estimated Al*	7117.7	0.06	1.83 2.00	40 46	0.73 0.18 *0.09 (12%)*	1.97 2.12	60 54	1.10 0.21 *0.69*
SP14, $Mgt_{0.81}$	Fe Mg *Estimated Al*	7117.9	0.06	1.84 2.00	35 42	0.85 0.09 *0.06 (16%)*	1.98 2.19	65 58	1.57 0.11 *0.32*

970
971

Table 3 Tetrahedral (Td) and octahedral (Oh) site occupancies calculated for 4 oxygens and based on Fe^{2+} and Fe^{3+} proportions determined by XMCD at room temperature (298 K) and for SP9 at 20 K.

Sample	$MgAl_2O_4$ (Mgt_0)	SP3 ($Mgt_{0.17}$)	SP5 ($Mgt_{0.23}$)	SP9 ($Mgt_{0.41}$) 298 K	20 K	SP50 ($Mgt_{0.51}$)	SP20 ($Mgt_{0.55}$)	SP13 ($Mgt_{0.61}$)	SP17 ($Mgt_{0.71}$)	SP14 ($Mgt_{0.81}$)	Fe_3 (Mg
Fe_3O_4 content	0.000	0.165	0.234	0.405		0.506	0.554	0.608	0.710	0.807	1.00
O pfu	4.000	4.000	4.000	4.000		4.000	4.000	4.000	4.000	4.000	4.00
Site occupancies: 10% total Al in Td											
A site (Td)											
Si		0.007	0.006	0.0005	(0.0005)*	0.003	0.0003	0.002	0.0007	n.d.	
Al	0.200	0.169	0.155	0.118	(0.118)	0.099	0.090	0.079	0.059	0.039	
Mg	0.800	0.699	0.636	0.402	(0.427)	0.264	0.248	0.182	0.144	0.094	
Fe^{2+} Td		0.000	0.000	0.028	(0.058)	0.081	0.072	0.068	0.036	0.000	0.00
Fe^{3+} Td		0.125	0.203	0.451	(0.396)	0.553	0.590	0.669	0.760	0.867	1.00
Total A	1.000	1.000	1.000	1.000	(1.000)	1.000	1.000	1.000	1.000	1.000	1.00
B-site (Oh)											
Al	1.800	1.523	1.399	1.065	(1.065)	0.895	0.813	0.714	0.532	0.348	
Mg	0.200	0.124	0.126	0.196	(0.170)	0.226	0.194	0.214	0.152	0.105	
Fe^{2+} Oh	-	0.241	0.325	0.345	(0.384)	0.456	0.535	0.700	0.876	0.916	1.00
Fe^{3+} Oh	-	0.129	0.173	0.394	(0.381)	0.431	0.473	0.421	0.507	0.670	1.00
Vacancy Oh	-	-	-	-		-	-	-	-	-	-
Total	2.000	2.017	2.023	2.000	(2.000)	2.008	2.015	2.049	2.067	2.039	2.00
Calc. A – O (Å)	1.922	1.916	1.913	1.905	(1.911)	1.903	1.902	1.898	1.893	1.888	1.88
Calc. B – O (Å)	1.928	1.951	1.962	1.984	(1.985)	1.997	2.004	2.018	2.033	2.042	2.06
Calc. *u*	0.2583	0.2609	0.2602	0.2589	(0.2590)	0.2587	0.2578	0.2570	0.2562	0.2555	0.25
Calc. *a* (Å)#	**8.086**	**8.143**	**8.169**	**8.217**	**(8.228)**	**8.249**	**8.266**	**8.297**	**8.331**	**8.349**	**8.39**
Meas. *a* (Å)	**8.085**	**8.141**	**8.169**	**8.233**		**8.262**	**8.268**	**8.293**	**8.322**	**8.346**	**8.39**
Calculated magnetic moment (Bohr)	**0**	**1.0(1)**	**1.2(1)**	**1.0(1)**	**1.25(9)**	**0.92(5)**	**1.29(5)**	**1.33(5)**	**2.14(6)**	**2.74(8)**	**4.06**

* Data based on XMCD spectrum measured at 20 K; # Estimated error ~0.005Å for all samples based on analytical data.

Table 4. Comparison of site occupancies from Nell and Wood (1989), Harrison et al. (1999) and this work. Calculated magnetic moments are given for each dataset and compared with measured saturation magnetisation.

	Nell and Wood, 1989 Data for 1000°C			Harrison et al.. 1999 Data for 1000°C			This paper					
							XMCD data at 25°C			Model 'high-T' pseudo-ran Mg, Fe^{2+}, Fe^{3+} with fixed		
	$Mgt_{0.75}$	$Mgt_{0.50}$	$Mgt_{0.25}$	$Mgt_{0.60}$ NS40	$Mgt_{0.50}$ NS50	$Mgt_{0.25}$ NS75	$Mgt_{0.61}$ SP13	$Mgt_{0.51}$ SP50	$Mgt_{0.23}$ SP9	$Mgt_{0.61}$ SP13	$Mgt_{0.51}$ SP50	Mg SP
Td site	A	B	C	D	E	F	G	H	I	J	K	L
Fe^{2+}	0.198	0.272	0.214	0.263	0.236	0.167	0.068	0.081	0	0.313	0.240	0.1
Fe^{3+}	0.728	0.634	0.453	0.534	0.418	0.195	0.669	0.553	0.203	0.444	0.439	0.2
Mg	0.071	0.068	0.286	0.178	0.236	0.508	0.182	0.264	0.636	0.162	0.219	0.4
Al	0.003	0.026	0.047	0.025	0.110	0.130	0.079	0.099	0.155	0.079	0.099	0.1
Total	1.000	1.000	1.000	1.000	1.000	1.000	1.000[$]	1.000[*]	1.000[+]	1.000[$]	1.000[*]	1.0
Oh site												
Fe^{2+}	0.558	0.244	0.028	0.307	0.264	0.083	0.700	0.456	0.325	0.455	0.298	0.1
Fe^{3+}	0.786	0.367	0.065	0.666	0.582	0.305	0.421	0.431	0.173	0.646	0.545	0.1
Mg	0.172	0.408	0.450	0.222	0.264	0.242	0.214	0.226	0.126	0.235	0.271	0.3
Al	0.484	0.981	1.457	0.775	0.890	1.370	0.714	0.895	1.399	0.714	0.895	1.3
Total	2.000	2.000	2.000	2.000	2.000	2.000	2.049	2.008	2.023	2.049	2.009	2.0
Calculated M_s	1.75	-1.45	-2.69	1.37	0.97	0.21	1.33	0.91	1.17	1.58	0.76	-0.
Measured M_s[&]				1.27	0.89	0.27						

[$] Includes Si 0.002; [*] Includes Si 0.003; [+] Includes Si 0.006; [&] Harrison and Putnis (1995)

Table 1. Analyses and cell formulae for synthetic $MgAl_2O_4$ – Fe_3O_4 solid solutions and XMCD data for Fe^{2+} and Fe^{3+} proportions at room T (298 K) and for SP9 at 20 K (i.e., below its Curie temperature).

	SP3	SP5	SP9		SP50	SP20	SP13	SP17	SP14
	Harrison & Putnis (1995)	Harrison & Putnis (1995)	This paper Average of 10		This paper Average of 12	This paper Average of 18	Harrison & Putnis (1995)	Harrison (1997)	Harrison (1997)
Fe_3O_4 (molecular %)	16.5(2)[%]	23.4(2)	40.5(5)		50.6(5)	55.4(6)	60.8(9)	71.0(5)	80.7(7)
Wt.%									
SiO_2	0.26[$](8)[%]	0.22[$](9)	0.02[$](1)		0.09(8)	0.01(1)	0.06[$](2)	0.02[$](2)	n.d.
Al_2O_3	55.4(6)	48.5(2)	34.1(5)		27.2(4)	23.9(7)	20.5(1.5)	14.3(3)	9.0(2)
Total Fe as FeO	23.0(2)	31.1(1)	49.4(5)		58.6(7)	62.4(8)	67.5(1.5)	74.3(3)	80.9(7)
Fe_2O_3[*]	15.6	22.3	36.7		43.0	45.9	50.0	55.0	60.1
FeO[*]	8.9	11.0	16.4		19.9	21.1	22.6	24.8	26.8
MgO	21.2(2)	18.9(1)	13.6(1)		10.6(3)	9.2(2)	8.1(3)	5.7(1)	3.7(1)
Total	101.4	100.9	100.8		100.8	100.1	101.2	99.8	99.6
Cats/4(O), 3cats									
Si	0.007(2)	0.006(2)	0.0005(2)		0.003(2)	0.0003(2)	0.002(1)	0.0007(6)	0.000
Al	1.68(2)[&]	1.537(6)	1.18(2)		0.993(14)	0.90(3)	0.78(6)	0.578(12)	0.381(9)
Fe^{3+}	0.303	0.451	0.814		1.002	1.100	1.216	1.420	1.619
Fe^{2+}	0.192	0.248	0.403		0.515	0.562	0.612	0.711	0.803
Mg	0.817(8)	0.758(4)	0.597(4)		0.487(13)	0.438(9)	0.390(14)	0.290(5)	0.197(5)
Total Fe atoms[&]	0.494(4)	0.699(15)	1.217(12)		1.517(18)	1.662(21)	1.83(4)	2.131(9)	2.42(2)
Atom $Fe^{3+}/(Fe^{3+}+Fe^{2+})$	0.612	0.645	0.669		0.661	0.662	0.665	0.666	0.669
Curie temp.(K)[+]	~20	~20	215		380	440	505	615	710
Cell edge, Å[^]	8.141(1)	8.169(1)	8.233(2)		8.262(2)	8.268(2)	8.293(2)	8.322(1)	8.346(2)
Cats/4(O) for XMCD Fe^{2+} and Fe^{3+} props.			298 K	20K					
Si	0.007(2)	0.006(2)	0.0005(2)	0.0005(2)	0.003(2)	0.0003(2)	0.002(1)	0.0007(6)	0.000
Al	1.69(2)	1.553(6)	1.18(2)	1.18(2)	0.994(14)	0.90(3)	0.79(6)	0.591(12)	0.387(9)
[#]Fe^{3+}	0.25(4)	0.37(4)	0.85(3)	0.78(2)	0.98(2)	1.06(2)	1.09(2)	1.27(2)	1.54(2)
[#]Fe^{2+}	0.24(4)	0.33(4)	0.37(3)	0.44(2)	0.54(2)	0.61(2)	0.77(2)	0.91(2)	0.92(2)
Mg	0.822(8)	0.763(15)	0.600(4)	0.600(4)	0.490(13)	0.442(9)	0.396(14)	0.296(5)	0.199(5)
Cation total	3.017	3.023	3.000	3.000	3.008	3.015	3.049	3.067	3.039
Total Fe atoms	0.495(4)	0.701(15)	1.218(12)	1.219(12)	1.521(18)	1.670(21)	1.86(4)	2.179(9)	2.45(2)
XMCD: Atom $Fe^{3+}/(Fe^{3+}+Fe^{2+})$	0.512	0.536	0.694	0.637	0.647	0.637	0.587	0.582	0.627

[$] SiO_2 concentrations determined for this paper; [%]Numbers in brackets are estimated 1 sigma errors for last place(s); [*] Calculated for 3 cations and 4 oxygens pfu; [+] From Harrison and Putnis (1996); [^] From Harrison and Putnis (1995; 1997); [&] Errors assumed to be the same as for wt.% analytical values; [#] Errors for XMCD determined Fe^{2+} and Fe^{3+} are 1-2% relative for Fe-rich ferrimagnetic samples and 5-10% for Fe-poor paramagnetic samples.

Table 2. K-edge EXAFS parameters for Fe and Mg in spinel - magnetite ($MgAl_2O_4$ – Fe_3O_4) solid solutions and fitted M – O bond lengths and cation occupancies for the tetrahedral and octahedral sites.

Sample	Element	K-edge energy, eV	Pre-edge/ Edge at ½ height	Tetrahedral Site Td			Octahedral Site, Oh		
				R, Å	Proportion in Td , %	Normalised occupancy	R, Å	Proportion in Oh, %	Normalised occupancy
SP5, $Mgt_{0.23}$	Fe Mg *Estimated Al*	7117.0	0.06	1.84 1.97	45 54	0.32 0.41 *0.27 (18%)*	1.97 2.12	55 46	0.38 0.35 *1.27*
SP9, $Mgt_{0.41}$	Fe Mg *Estimated Al*	7117.0	0.06	1.84 2.00	45 47	0.52 0.28 *0.20 (16%)*	1.96 2.10	55 53	0.64 0.32 *1.04*
SP50, $Mgt_{0.51}$	Fe Mg *Estimated Al*	7117.3	0.06	1.83 2.00	40 45	0.61 0.23 *0.15 (15%)*	1.97 2.06	60 55	0.91 0.28 *0.81*
SP13, $Mgt_{0.61}$	Fe Mg *Estimated Al*	7117.7	0.06	1.83 2.00	40 46	0.73 0.18 *0.09 (12%)*	1.97 2.12	60 54	1.10 0.21 *0.69*
SP14, $Mgt_{0.81}$	Fe Mg *Estimated Al*	7117.9	0.06	1.84 2.00	35 42	0.85 0.09 *0.06 (16%)*	1.98 2.19	65 58	1.57 0.11 *0.32*

Table 3 Tetrahedral (Td) and octahedral (Oh) site occupancies calculated for 4 oxygens and based on Fe^{2+} and Fe^{3+} proportions determined by XMCD at room temperature (298 K) and for SP9 at 20 K.

Sample	$MgAl_2O_4$ (Mgt_0)	SP3 ($Mgt_{0.17}$)	SP5 ($Mgt_{0.23}$)	SP9 ($Mgt_{0.41}$) 298 K	20 K	SP50 ($Mgt_{0.51}$)	SP20 ($Mgt_{0.55}$)	SP13 ($Mgt_{0.61}$)	SP17 ($Mgt_{0.71}$)	SP14 ($Mgt_{0.81}$)	Fe_3O_4 ($Mgt_{1.0}$)
Fe_3O_4 content	0.000	0.165	0.234	0.405		0.506	0.554	0.608	0.710	0.807	1.000
O pfu	4.000	4.000	4.000	4.000		4.000	4.000	4.000	4.000	4.000	4.000
Site occupancies: 10% total Al in Td											
A site (Td)											
Si		0.007	0.006	0.0005	(0.0005)*	0.003	0.0003	0.002	0.0007	n.d.	
Al	0.200	0.169	0.155	0.118	(0.118)	0.099	0.090	0.079	0.059	0.039	
Mg	0.800	0.699	0.636	0.402	(0.427)	0.264	0.248	0.182	0.144	0.094	
Fe^{2+} Td		0.000	0.000	0.028	(0.058)	0.081	0.072	0.068	0.036	0.000	0.000
Fe^{3+} Td		0.125	0.203	0.451	(0.396)	0.553	0.590	0.669	0.760	0.867	1.000
Total A	1.000	1.000	1.000	1.000	(1.000)	1.000	1.000	1.000	1.000	1.000	1.000
B-site (Oh)											
Al	1.800	1.523	1.399	1.065	(1.065)	0.895	0.813	0.714	0.532	0.348	
Mg	0.200	0.124	0.126	0.196	(0.170)	0.226	0.194	0.214	0.152	0.105	
Fe^{2+} Oh	-	0.241	0.325	0.345	(0.384)	0.456	0.535	0.700	0.876	0.916	1.000
Fe^{3+} Oh	-	0.129	0.173	0.394	(0.381)	0.431	0.473	0.421	0.507	0.670	1.000
Vacancy Oh	-	-	-	-		-	-	-	-	-	-
Total	2.000	2.017	2.023	2.000	(2.000)	2.008	2.015	2.049	2.067	2.039	2.000
Calc. A – O (Å)	1.922	1.916	1.913	1.905	(1.911)	1.903	1.902	1.898	1.893	1.888	1.885
Calc. B – O (Å)	1.928	1.951	1.962	1.984	(1.985)	1.997	2.004	2.018	2.033	2.042	2.060
Calc. *u*	0.2583	0.2609	0.2602	0.2589	(0.2590)	0.2587	0.2578	0.2570	0.2562	0.2555	0.2547
Calc. *a* (Å)#	**8.086**	**8.143**	**8.169**	**8.217**	**(8.228)**	**8.249**	**8.266**	**8.297**	**8.331**	**8.349**	**8.393**
Meas. *a* (Å)	**8.085**	**8.141**	**8.169**	**8.233**		**8.262**	**8.268**	**8.293**	**8.322**	**8.346**	**8.396**
Calculated magnetic moment (Bohr)	**0**	**1.0(1)**	**1.2(1)**	**1.0(1)**	**1.25(9)**	**0.92(5)**	**1.29(5)**	**1.33(5)**	**2.14(6)**	**2.74(8)**	**4.06**

* Data based on XMCD spectrum measured at 20 K; # Estimated error ~0.005Å for all samples based on analytical data.

Table 4. Comparison of site occupancies from Nell and Wood (1989), Harrison et al. (1999) and this work. Calculated magnetic moments are given for each dataset and compared with measured saturation magnetisation.

	Nell and Wood, 1989 Data for 1000°C			Harrison et al.. 1999 Data for 1000°C			This paper								
							XMCD data at 25°C			Model 'high-T' pseudo-random Mg, Fe^{2+}, Fe^{3+} with fixed Al			Model 'high-T' with $Fe^{2+}_{Td} = 0.333Fe^{2+}_{Total}$		
	$Mgt_{0.75}$	$Mgt_{0.50}$	$Mgt_{0.25}$	$Mgt_{0.60}$ NS40	$Mgt_{0.50}$ NS50	$Mgt_{0.25}$ NS75	$Mgt_{0.61}$ SP13	$Mgt_{0.51}$ SP50	$Mgt_{0.23}$ SP9	$Mgt_{0.61}$ SP13	$Mgt_{0.51}$ SP50	$Mgt_{0.23}$ SP9	$Mgt_{0.61}$ SP13	$Mgt_{0.51}$ SP50	$Mgt_{0.23}$ SP9
Td site	A	B	C	D	E	F	G	H	I	J	K	L	M	N	O
Fe^{2+}	0.198	0.272	0.214	0.263	0.236	0.167	0.068	0.081	0	0.313	0.240	0.186	0.253	0.177	0.107
Fe^{3+}	0.728	0.634	0.453	0.534	0.418	0.195	0.669	0.553	0.203	0.444	0.439	0.216	0.484	0.457	0.096
Mg	0.071	0.068	0.286	0.178	0.236	0.508	0.182	0.264	0.636	0.162	0.219	0.436	0.182	0.264	0.635
Al	0.003	0.026	0.047	0.025	0.110	0.130	0.079	0.099	0.155	0.079	0.099	0.155	0.079	0.099	0.155
Total	1.000	1.000	1.000	1.000	1.000	1.000	1.000$^{\$}$	1.000*	1.000^{+}	1.000$^{\$}$	1.000*	1.000^{+}	1.000$^{\$}$	1.000*	1.000^{+}
Oh site															
Fe^{2+}	0.558	0.244	0.028	0.307	0.264	0.083	0.700	0.456	0.325	0.455	0.298	0.140	0.515	0.360	0.218
Fe^{3+}	0.786	0.367	0.065	0.666	0.582	0.305	0.421	0.431	0.173	0.646	0.545	0.162	0.606	0.527	0.280
Mg	0.172	0.408	0.450	0.222	0.264	0.242	0.214	0.226	0.126	0.235	0.271	0.326	0.214	0.226	0.129
Al	0.484	0.981	1.457	0.775	0.890	1.370	0.714	0.895	1.399	0.714	0.895	1.396	0.714	0.895	1.396
Total	2.000	2.000	2.000	2.000	2.000	2.000	2.049	2.008	2.023	2.049	2.009	2.023	2.049	2.008	2.023
Calculated M_s	1.75	-1.45	-2.69	1.37	0.97	0.21	1.33	0.91	1.17	1.58	0.76	-0.46	1.67	1.10	1.37
Measured M_s[&]				1.27	0.89	0.27									

$^{\$}$ Includes Si 0.002; * Includes Si 0.003; $^{+}$ Includes Si 0.006; [&] Harrison and Putnis (1995)

XMCDFigure1

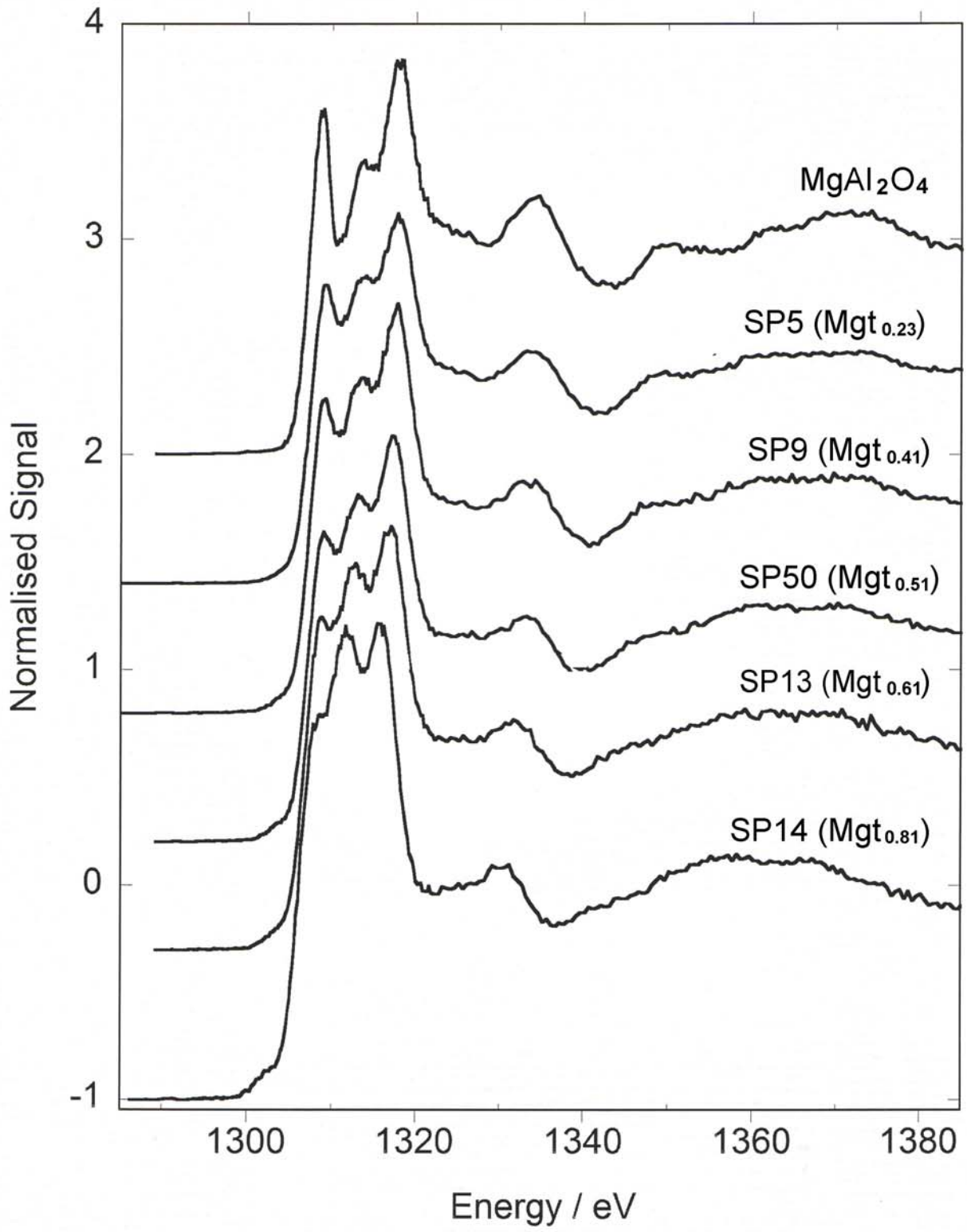

Figure 2

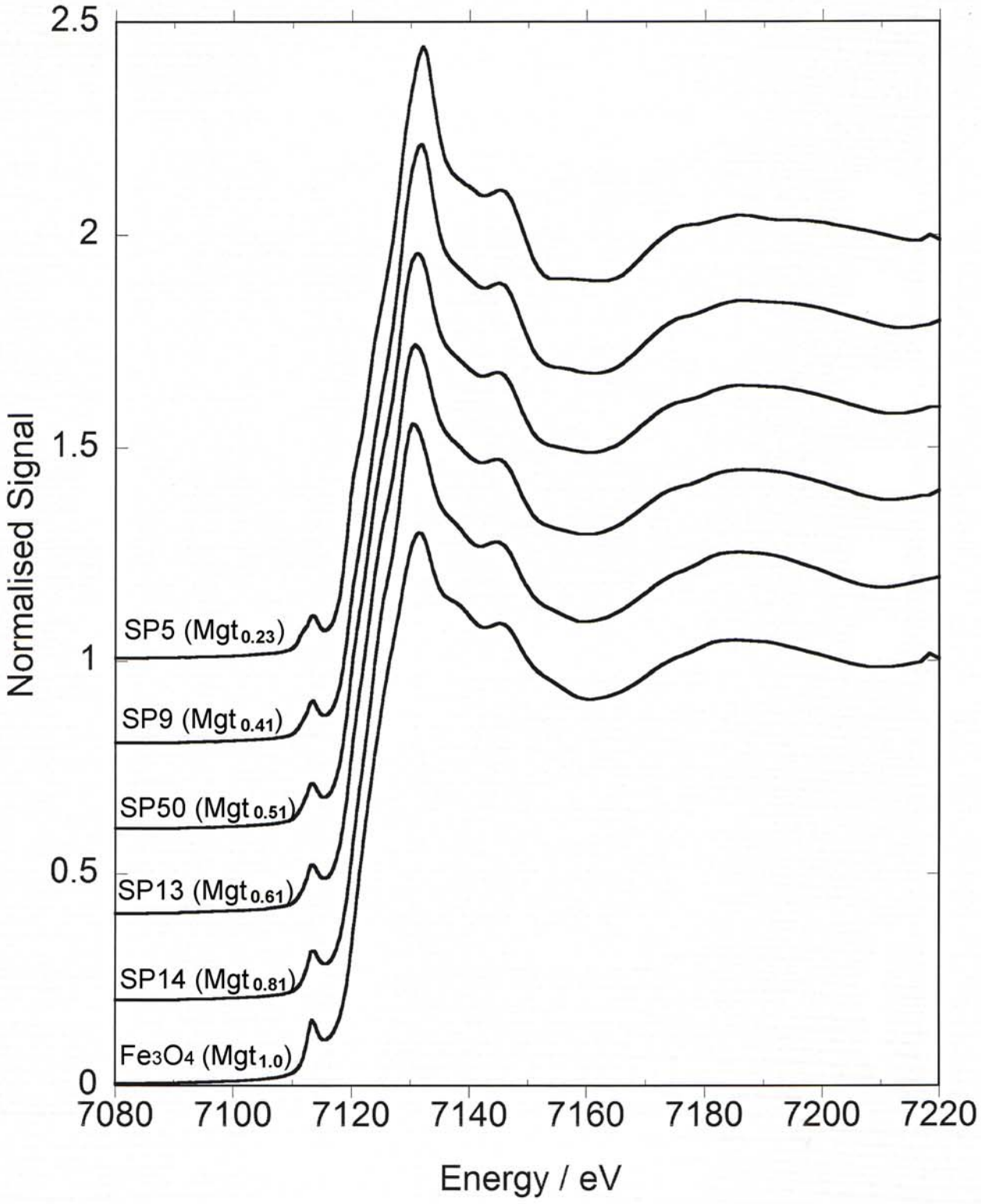
2.5
2
1.5
1
0.5
0
Normalised Signal
SP5 (Mgt0.23)
SP9 (Mgt0.41)
SP50 (Mgt0.51)
SP13 (Mgt0.61)
SP14 (Mgt0.81)
Fe3O4 (Mgt1.0)
7080
7100
7120
7140
7160
7180
7200
7220
Energy / eV

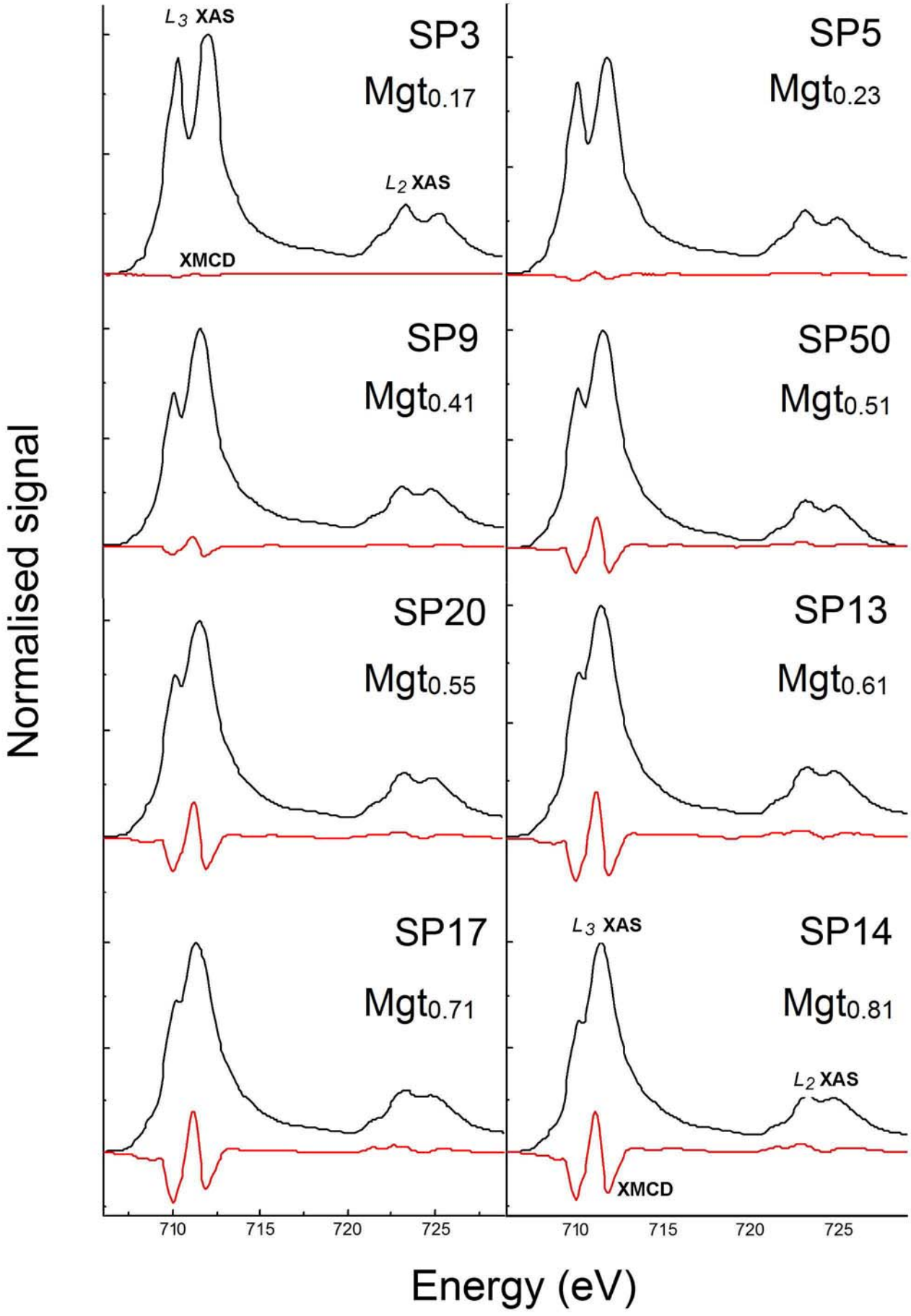
Normalised signal
Energy (eV)
SP3
Mgt0.17
SP5
Mgt0.23
SP9
Mgt0.41
SP50
Mgt0.51
SP20
Mgt0.55
SP13
Mgt0.61
SP17
Mgt0.71
SP14
Mgt0.81
L3 XAS
L2 XAS
XMCD
710
715
720
725

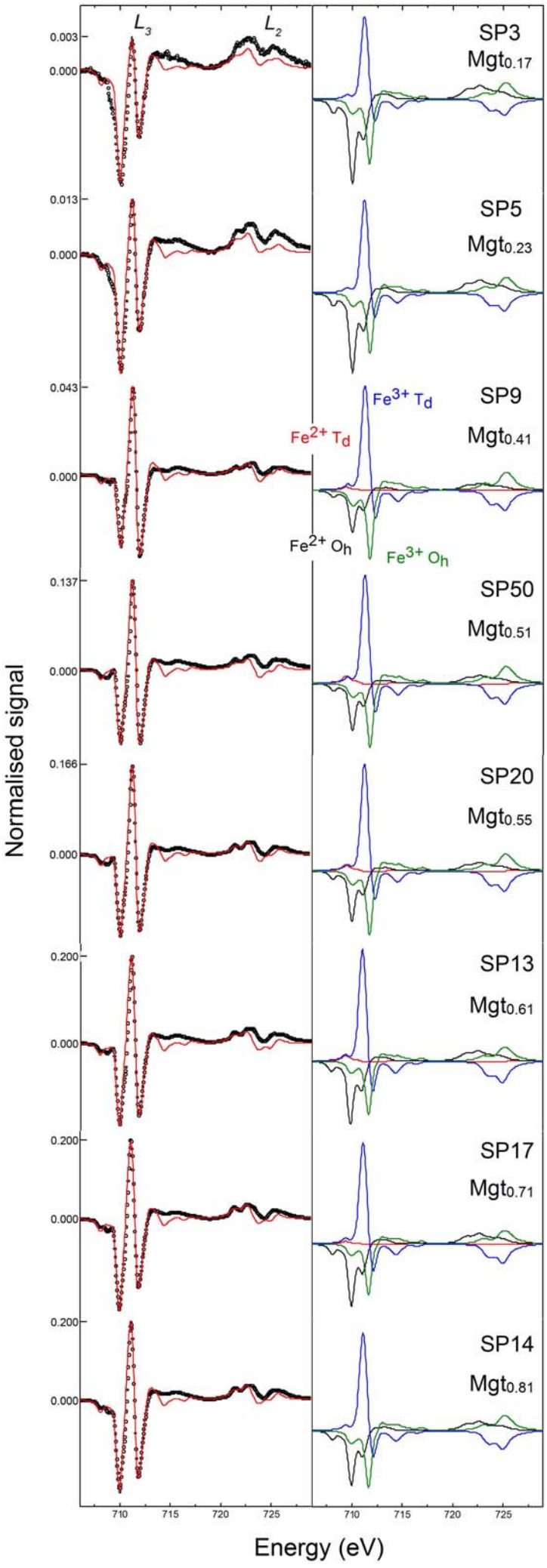
L_3
L_2
SP3
$Mgt_{0.17}$
SP5
$Mgt_{0.23}$
SP9
$Mgt_{0.41}$
Fe^{3+} Td
Fe^{2+} Td
Fe^{2+} Oh
Fe^{3+} Oh
SP50
$Mgt_{0.51}$
SP20
$Mgt_{0.55}$
SP13
$Mgt_{0.61}$
SP17
$Mgt_{0.71}$
SP14
$Mgt_{0.81}$
0.003
0.000
0.013
0.000
0.043
0.000
0.137
0.000
0.166
0.000
0.200
0.000
0.200
0.000
0.200
0.000
710
715
720
725
Normalised signal
Energy (eV)

Figure 5

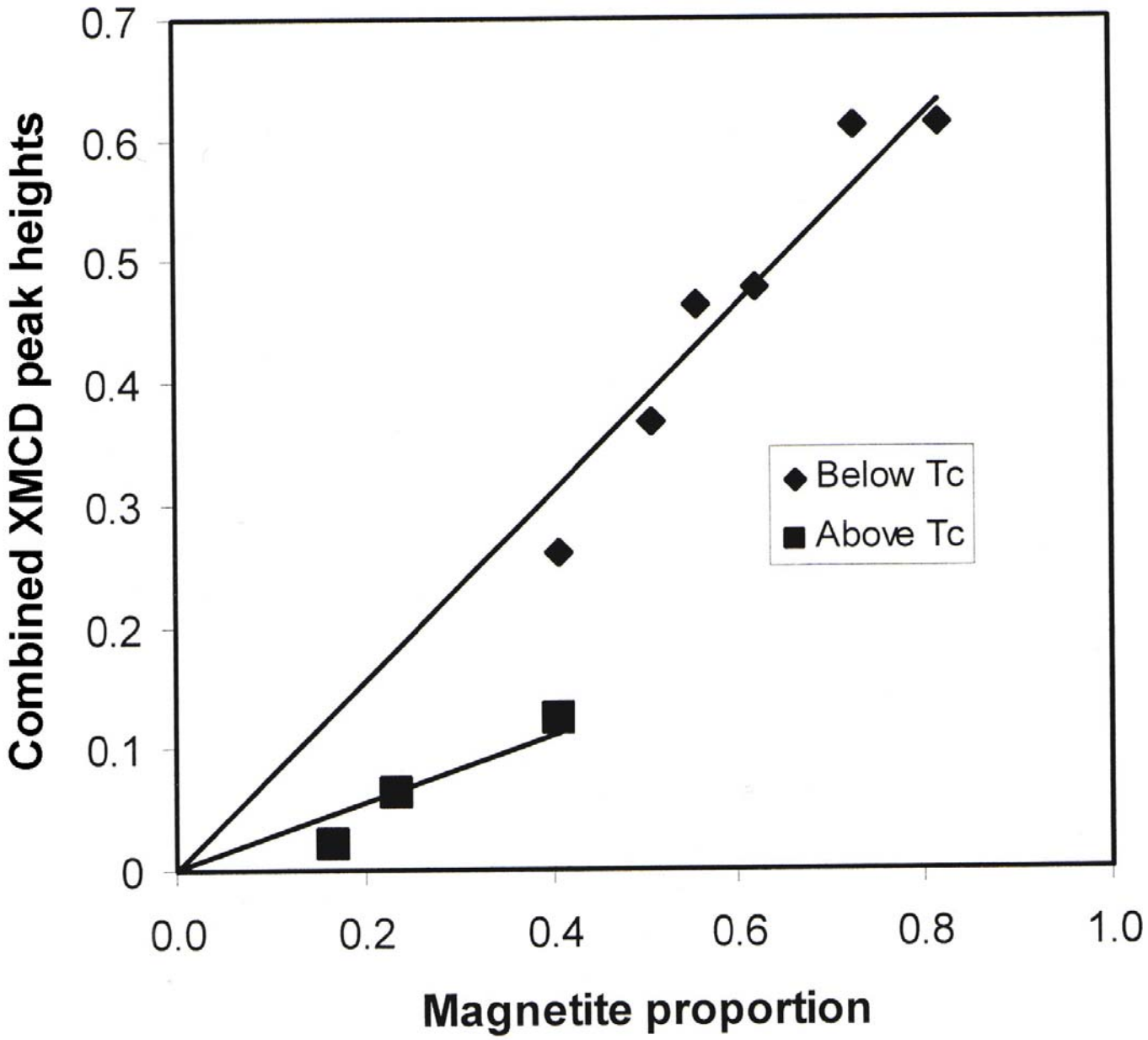
Combined XMCD peak heights
0.7
0.6
0.5
0.4
0.3
0.2
0.1
0
0.0
0.2
0.4
0.6
0.8
1.0
Magnetite proportion
Below Tc
Above Tc

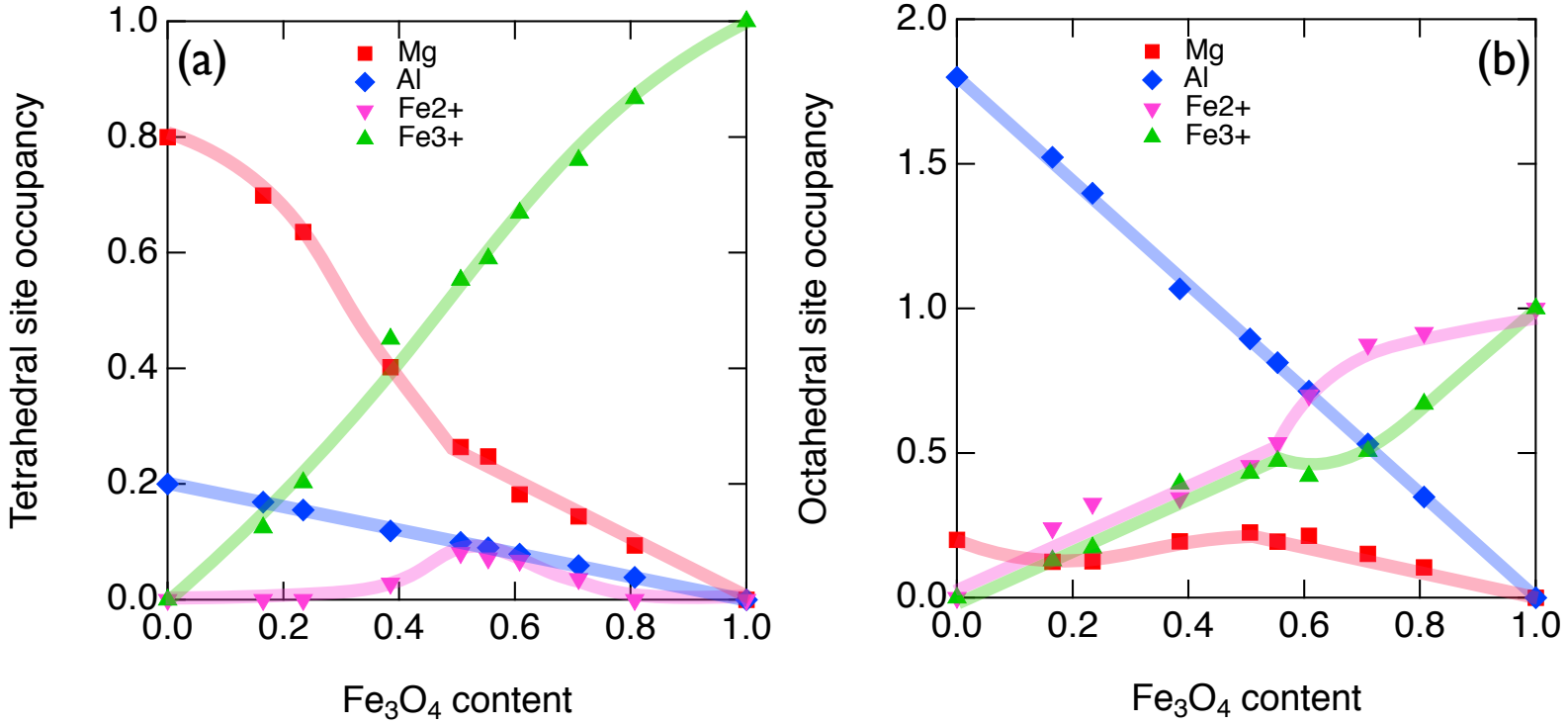
(a)
Mg
Al
Fe2+
Fe3+
Tetrahedral site occupancy
1.0
0.8
0.6
0.4
0.2
0.0
0.0
0.2
0.4
0.6
0.8
1.0
Fe3O4 content
(b)
Mg
Al
Fe2+
Fe3+
Octahedral site occupancy
2.0
1.5
1.0
0.5
0.0
0.0
0.2
0.4
0.6
0.8
1.0
Fe3O4 content

Fig. 6

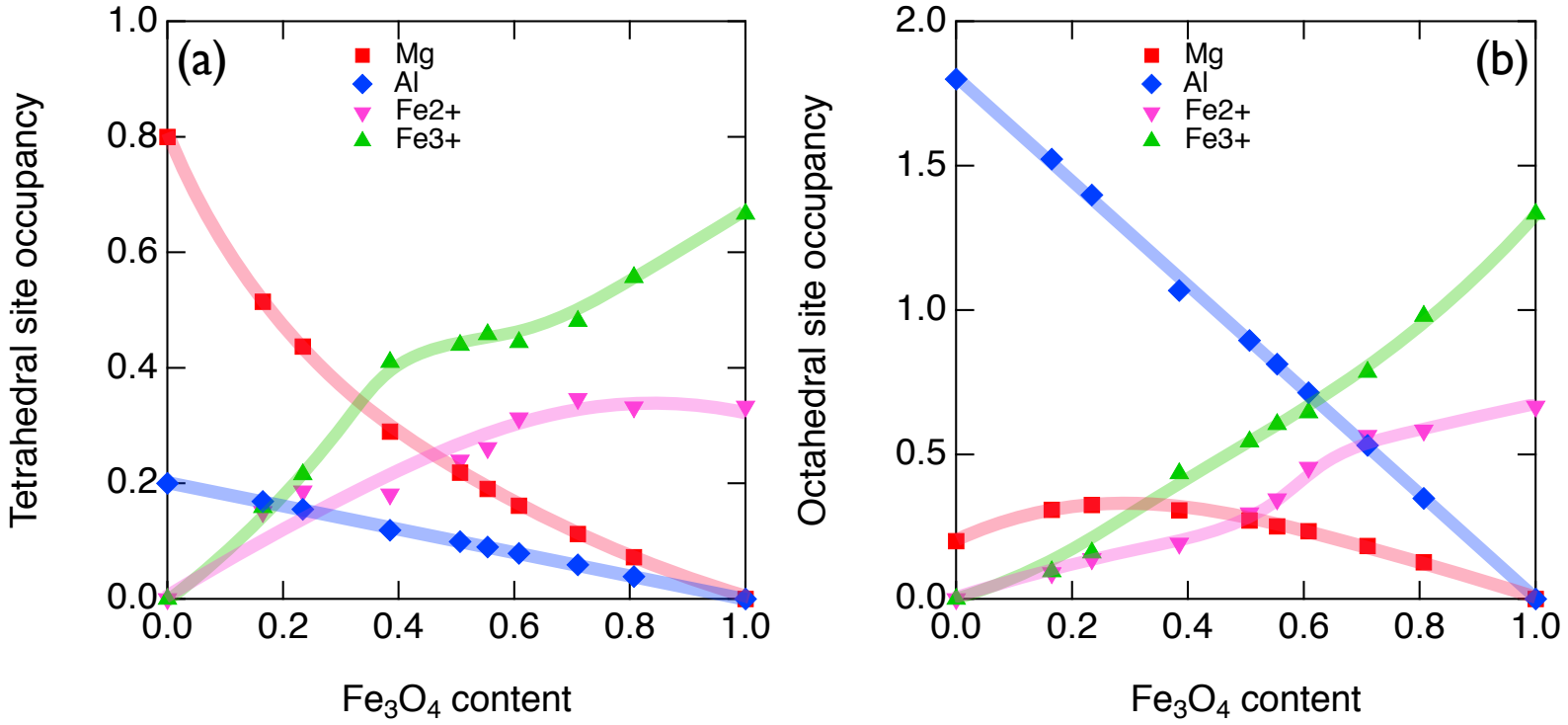
(a)
Mg
Al
Fe2+
Fe3+
Tetrahedral site occupancy
1.0
0.8
0.6
0.4
0.2
0.0
0.0
0.2
0.4
0.6
0.8
1.0
Fe3O4 content
(b)
Mg
Al
Fe2+
Fe3+
Octahedral site occupancy
2.0
1.5
1.0
0.5
0.0
0.0
0.2
0.4
0.6
0.8
1.0
Fe3O4 content

Fig. 7

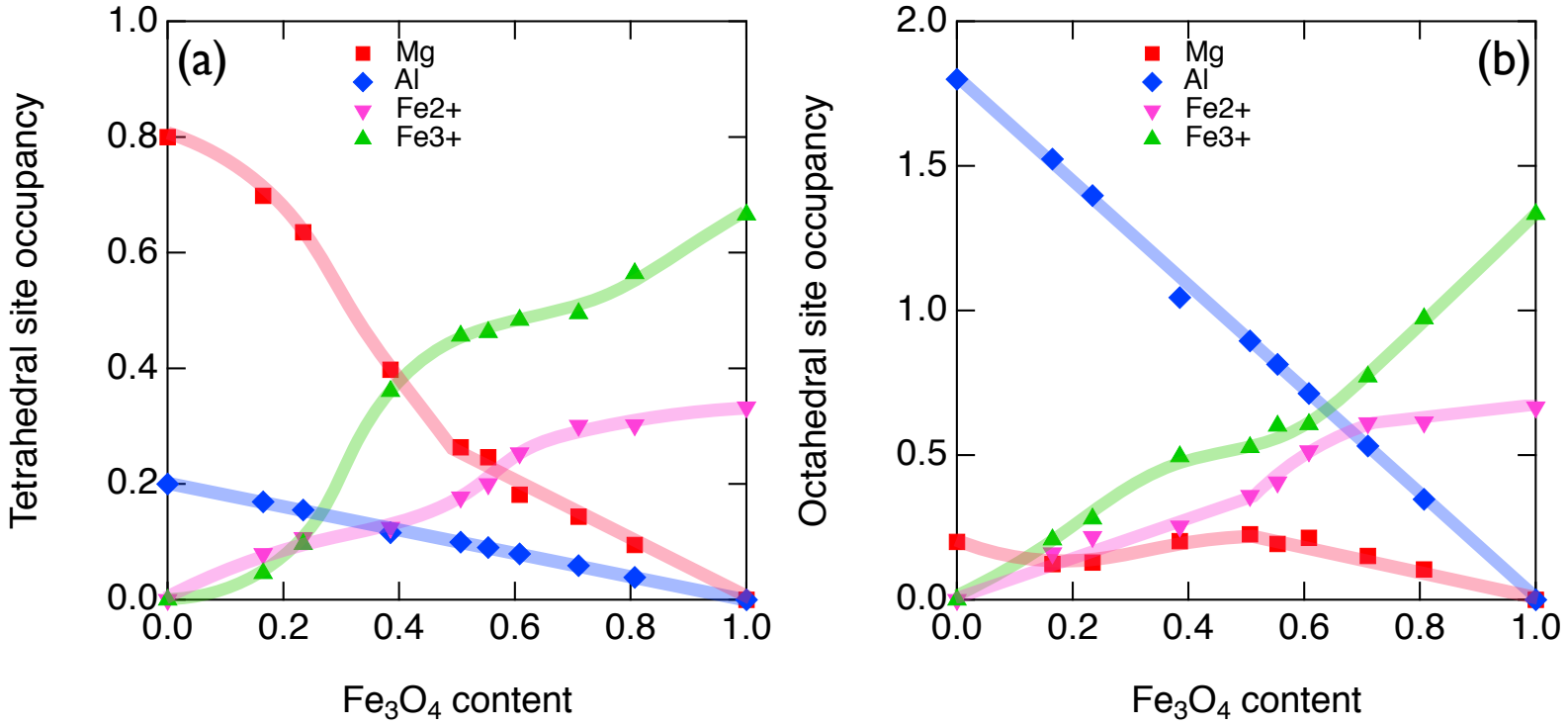
(a)
Mg
Al
Fe2+
Fe3+
Tetrahedral site occupancy
1.0
0.8
0.6
0.4
0.2
0.0
0.0
0.2
0.4
0.6
0.8
1.0
Fe3O4 content
(b)
Mg
Al
Fe2+
Fe3+
Octahedral site occupancy
2.0
1.5
1.0
0.5
0.0
0.0
0.2
0.4
0.6
0.8
1.0
Fe3O4 content

Fig. 8

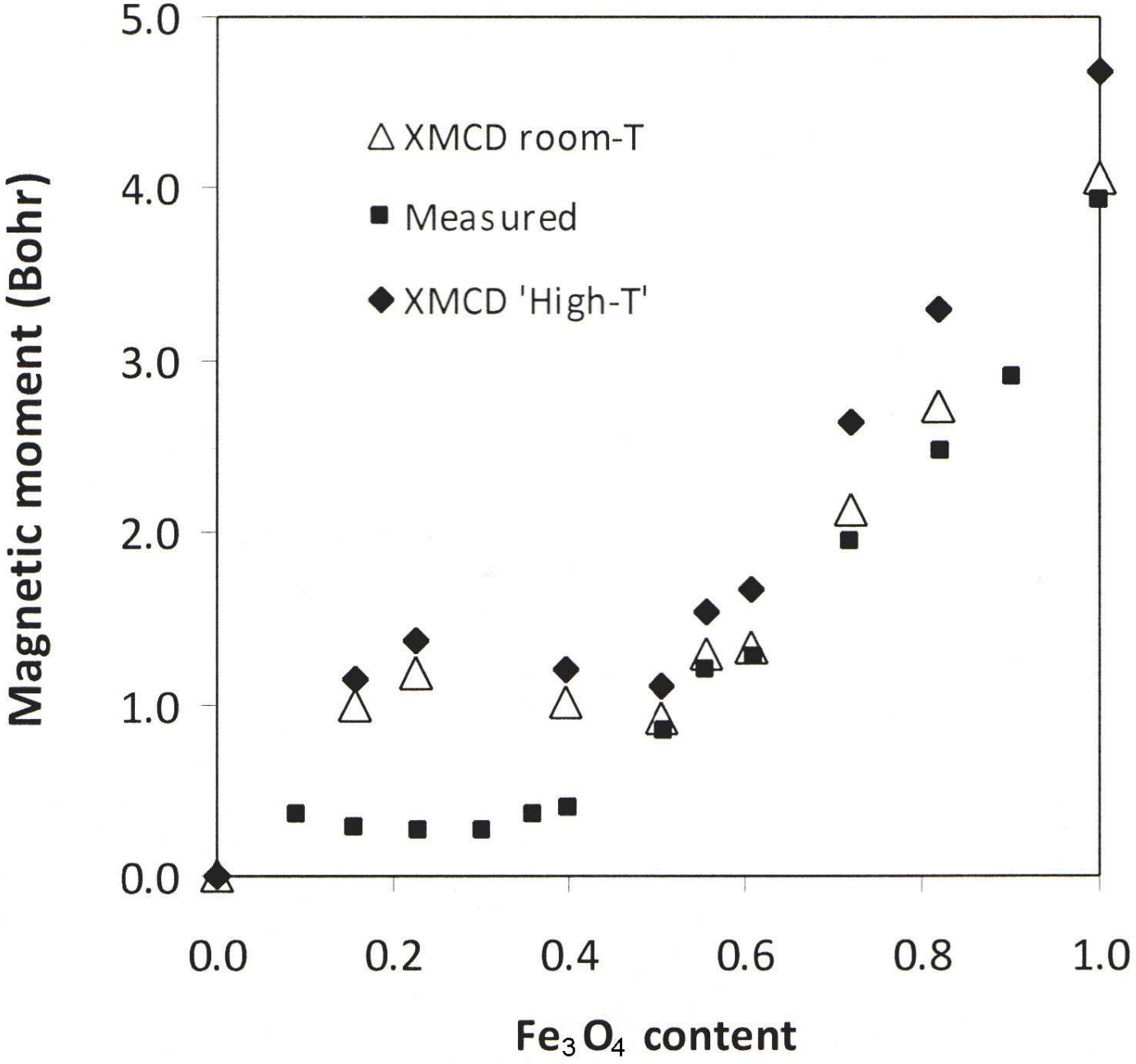
5.0
4.0
3.0
2.0
1.0
0.0
Magnetic moment (Bohr)
△ XMCD room-T
■ Measured
◆ XMCD 'High-T'
0.0
0.2
0.4
0.6
0.8
1.0
Fe3O4 content